Chromatin remodeling protein CHD4 regulates axon guidance of spiral ganglion neurons in developing cochlea

Jihyun Kim[1,2,*], Edward Martinez[1,2,*], Jingyun Qiu[2], Julie Zhouli Ni[3], Kelvin Y. Kwan[1,2]

[1]Keck Center for Collaborative Neuroscience and Stem Cell Research Center, Rutgers University, Piscataway, NJ 08854, USA

[2]Department of Cell Biology and Neuroscience, Rutgers University, Piscataway, NJ 08854, USA

[3] Department of Molecular Biology and Biochemistry, Rutgers University, Piscataway, NJ 08854, USA

* J.K. and E.M. contributed equally to this work.

Corresponding Author:

Kelvin Y. Kwan

Address: 604 Allison Road, D250 Nelson Labs, Piscataway, NJ 08854

Email: kwan@dls.rutgers.edu

Running Title: CHD4 axon guidance

Key Words: CHD4, spiral ganglion neurons, axon guidance, epigenetics, chromatin remodeling

Word Count:

Number of Figures: 6

Number of Tables: 3

Number of Supplemental Figures: 3

Number of Supplemental Table: 1

Abstract (202 words)

The chromodomain helicase binding protein 4 (CHD4) is an ATP-dependent chromatin remodeler. *De-novo* pathogenic variants of *CHD4* cause Sifrim-Hitz-Weiss syndrome (SIHIWES). Patients with SIHIWES show delayed development, intellectual disability, facial dysmorphism, and hearing loss. Many cochlear cell types, including spiral ganglion neurons (SGNs), express CHD4. SGNs are the primary afferent neurons that convey sound information from the cochlea, but the function of CHD4 in SGNs is unknown. We employed the Neurog1(Ngn1) CreERT^2 *Chd4* conditional knockout animals to delete *Chd4* in SGNs. SGNs are classified as type I and type II neurons. SGNs lacking CHD4 showed abnormal fasciculation of type I neurons along with improper pathfinding of type II fibers. CHD4 binding to chromatin from immortalized multipotent otic progenitor-derived neurons was used to identify candidate target genes in SGNs. Gene ontology analysis of CHD4 target genes revealed cellular processes involved in axon guidance, axonal fasciculation, and ephrin receptor signaling pathway. We validated increased *Epha4* transcripts in SGNs from *Chd4* conditional knockout cochleae. The results suggest that CHD4 attenuates the transcription of axon guidance genes to form the stereotypic pattern of SGN peripheral projections. The results implicate epigenetic changes in circuit wiring by modulating axon guidance molecule expression and provide insights into neurodevelopmental diseases.

16 **Introduction**

17

18 Congenital hearing loss syndromes are often associated with pathogenic genetic variants in a single
19 gene. Hearing loss can be syndromic or non-syndromic. Syndromic hearing impairment is associated
20 with clinical features in other organ systems, while non-syndromic hearing impairment has no discernable
21 clinical abnormalities other than in the middle or inner ear. Syndromic hearing loss accounts for over 400
22 genetic syndromic hearing loss conditions (Toriello et al., 2004). The characteristics of syndromic hearing
23 loss vary among the different syndromes and affect hearing in either one or both ears. The extent of
24 hearing loss varies dramatically and can range from profound to mild. Different syndromes show distinct
25 features of hearing loss at different sound frequencies. Improper development or dysfunction of the
26 sensory cells and neurons of the inner ear correlates to many forms of syndromic hearing loss.

27 Mutations in genes that code for epigenetic modifiers can cause syndromic hearing loss. Pathogenic
28 variants in DNA methyltransferases (DNMT1), histone methyltransferases (EHMT1, KMT2D),
29 acetyltransferase (KAT6B), and the chromodomain helicase DNA binding (CHD) protein family are
30 associated with hearing loss (Layman and Zuo, 2014). The CHD family of proteins mobilizes and
31 rearranges nucleosomes to alter chromatin accessibility. Pathogenic variants in CHD4 and CHD7 are
32 associated with Sifrim-Hitz-Weiss and CHARGE syndrome, respectively (Clapier et al., 2017; Micucci et
33 al., 2015). Sifrim-Hitz-Weiss (SIHIWES) is an autosomal dominant intellectual developmental disorder
34 with variable congenital abnormalities. Patients with SIHIWES show delayed development, intellectual
35 disability, facial dysmorphism, and ear abnormalities, including hearing loss (Sifrim et al., 2016a; Weiss
36 et al., 2016). Hearing loss in patients with SIHIWES is confounded by the potential function of CHD4 in
37 many different inner ear cell types during development. In the mouse, the expression of CHD4 and
38 components of the nucleosome remodeling and deacetylase (NuRD) complex are expressed in many
39 cells in the cochlea sensory epithelium (Layman et al., 2013). CHD4 has been studied in the context of
40 the NuRD complex (Tong et al., 1998; Xue et al., 1998; Zhang et al., 1998). Paralogs from six protein

41 families form the core NuRD complex (Millard et al., 2016; Torchy et al., 2015). Multiple paralogs from
42 each protein family can form distinct NuRD complexes (Torrado et al., 2017). The ATP-dependent
43 nucleosome remodeler CHD4 and the histone deacetylases (HDAC1, HDAC2) form the catalytic
44 subunits. Other members include the methyl binding proteins (MBD2, MBD3), and structural subunits
45 (MTA1, MTA2, MTA3, GATAD2A, GATAD2B, RBBP4, RBBP7). The NuRD complex is localized to active
46 promoters and enhancers to attenuate transcription (Morra et al., 2012; Watson et al., 2012).
47
48 A decrease in transcription caused by the NuRD complex affects a myriad of cellular processes, including
49 maintenance of cell identity, DNA damage repair, cell cycle progression, and cancer (Bornelov et al.,
50 2018; Hosokawa et al., 2013; Hung et al., 2012; Pan et al., 2012; Polo et al., 2010; Xia et al., 2017; Yang
51 et al., 2016). CHD4 binds to thousands of sites in the mammalian genome in a cell-type-specific manner,
52 and studies show that CHD4 forms distinct protein complexes with NuRD-independent functions
53 (Hoffmeister et al., 2017; Low et al., 2016). We employed a conditional knockout model to understand
54 CHD4 function in developing spiral ganglion neurons (SGNs) and how the deletion of CHD4 contributes
55 to hearing loss. SGNs are the primary afferent neurons in the cochlea that convey auditory signals from
56 the sensory hair cells to the cochlear nucleus in the brainstem. Improper function of SGNs could result
57 in sensorineural hearing loss. We examined *Chd4* function in SGNs using a transgenic mouse line
58 harboring the Neurog1(Ngn1) CreER^{T2} (Koundakjian et al., 2007), *Chd4* conditional knockout (cKO)
59 alleles (Williams et al., 2004) and a tdTomato reporter (Madisen et al., 2010).

Materials and Methods

Generation of *Chd4* conditional knockout mice

All procedures were based on institutional animal care, used committee research guidelines, and were done at Rutgers University. *Chd4*$^{tm1Kge/tm1Kge}$ (*Chd4* floxed*)* animals (RRID:MGI:3713386) were obtained from Dr. Katia Georgopoulos ((Williams et al., 2004). Neurog1(Ngn1) CreER^{T2} animals and Ai9 R26R tdTomato reporter animals were purchased from Jackson Laboratory (RRID:IMSR_JAX:008529 and RRID:IMSR_JAX:007909, respectively) (Koundakjian et al., 2007; Madisen et al., 2010). PCR genotyping was performed using the EconoTaq Plus Green 2X Master Mix (Lucigen) and primer pairs for wild-type and *Chd4* floxed alleles (Table 1). For Cre-induced excision of loxP-flanked exons that code for the ATPase domain of *Chd4*, a mixture of tamoxifen and β-estradiol was diluted in corn oil. β-estradiol was included to help alleviate the anti-estrogen effects of tamoxifen treatments. 1 mg of tamoxifen per 40 g of body weight was used on individual animals. Tamoxifen doses for pregnant female mice were adjusted for maternal body weight. Pregnant dams were gavaged with 0.25mg/40g of tamoxifen (Sigma #T5648) and 0.25µg/40g of β-estradiol (Sigma #E8875) daily on embryonic days (E) 8.5- 10.5 to induce Cre activity. For staging timed embryos, the morning that vaginal plugs were observed, pregnant female mice were considered carrying E 0.5 embryos.

Tissue fixation and preparation

Embryos or postnatal pups were sacrificed for inner ear dissection. After bisecting the mouse head, brain tissue was removed. The temporal bone was removed, and the inner ear was separated from other tissue and fixed directly in 4% formaldehyde in 1X PBS overnight at 4°C. To obtain cochlear epithelium, extraneous tissue and bone surrounding the cochlea were removed to obtain the cochlea duct. Reissner's membrane was removed to expose the sensory epithelium. The microdissected sensory epithelia were fixed in 4% formaldehyde containing 1X PBS overnight and washed with 1X PBS before being processed

85 for immunostaining and *in situ* hybridization. After processing, the cochlea, including spiral ganglion and
86 sensory epithelium, was flat-mounted.
87
88 **Immunohistochemistry**
89 The micro-dissected cochlea tissues fixed in 4% formaldehyde in 1X PBS were permeabilized in wash
90 buffer (1X PBS with 0.1% Triton X-100) for 10 min before incubated for at least 1 hour in blocking buffer
91 (1X PBS with 0.1% Triton X-100 and 5% normal goat serum) at room temperature. Samples were
92 incubated overnight at 4°C with appropriate primary antibodies diluted in the blocking solution. Samples
93 were then washed 3X for 10 min 1X PBS and incubated with the appropriate combinations of DAPI (1
94 µg/ml), Alexa Fluor 488 (1:500 dilution), Alexa Fluor 568 (1:500 dilution) or Alexa Fluor 647 (1:500
95 dilution) conjugated secondary antibodies (Life Technologies) for 2 hours at room temperature and rinsed
96 in wash buffer before mounting in Prolonged Gold Antifade (Life Technologies).
97
98 iMOP cells were fixed in 4% formaldehyde in 1X PBS for 20 minutes, permeabilized in wash buffer for
99 10 min, incubated in blocking buffer (1X PBS, 10% goat serum and 0.1% Triton X-100) for 1 hour and
100 incubated overnight with the primary antibodies in blocking buffer. Cells were incubated with primary
101 antibodies, rinsed in wash buffer and incubated with appropriate combinations of DAPI (1 µg/ml), Alexa
102 Fluor 488, Alexa Fluor 568 or Alexa Fluor 647 conjugated secondary antibodies (Life Technologies) in
103 blocking buffer for 2 hours. Samples were washed with 1X PBS and mounted in Prolonged Gold Antifade
104 (Life Technologies). All antibodies are listed in Table 2.
105
106 **Single-molecule *in situ* hybridization**
107 Single-molecule fluorescence in situ hybridization (smFISH) was performed using RNAscope (Wang et
108 al., 2012). The RNAscope multiplex fluorescent reagent kit version 2 (Advanced Cell Diagnostics) was
109 used to detect target RNAs according to the manufacturer's instructions. RNAscope probes are listed in
110 Table 3. Immunohistochemistry to enhance and detect tdTomato protein was performed after the smFISH

111 protocol. Samples were incubated in blocking buffer (1X PBS, 10% goat serum and 0.3% Triton X-100)
112 for 1 hour at room temperature, followed by overnight incubation with rabbit anti-RFP (Rockland) in
113 blocking buffer at 4°C. After incubation with primary antibodies, samples were washed with 1x PBS and
114 incubated with appropriate combinations of DAPI (1 µg/ml) and Alexa Fluor 568 conjugated secondary
115 antibodies (Life Technologies) in a blocking buffer for 2 hours at room temperature. Samples were
116 washed with 1X PBS and mounted in Prolonged Gold Antifade (Life Technologies).
117
118 **Fluorescence micrograph acquisition and visualization**
119 Samples were mounted on a 1.5-cover glass and acquired on a Zeiss LSM800 point scanning confocal
120 microscope. Antibody-conjugated fluorophores and tdTomato fluorescent protein were excited using four
121 laser lines (405,488, 561, and 633nm). 1024X1024 images were acquired using either the 40X (1.4 NA)
122 or 63X (1.4 NA) objective with 1.5-2x digital zoom and 4X Kalmann averaging. The brightness and
123 contrast on images were adjusted and viewed using Zen Blue (Zeiss).
124
125 **Cell Culture for iMOP cells**
126 iMOP cells were grown in suspension with DMEM/F12 (Life Technologies) containing B27 supplement
127 (Life Technologies), 25 µg/ml carbenicillin and 20 ng/ml bFGF (PeproTech). Cells were passaged weekly
128 by dissociation with TrpLE Express (Life Technologies), harvested by centrifugation and resuspended in
129 fresh medium. To generate iMOP-derived neurons, tissue culture dishes were coated with 10 µg/mL of
130 poly-D-lysine for 1 hour aspirated and allowed to dry for 15 min, coated overnight with 10 µg/mL of laminin
131 at 37°C, washed 3 times with 1X PBS before plating cells. Proliferating iMOP cultures were dissociated
132 in TrypLE Express (Life Technologies), resuspended in neurobasal media and counted using a Moxi
133 counter. Particles between 9-16 um were considered cells, and 1.5-2 $X10^4$ cells were seeded in a poly-
134 D-lysine and laminin-coated well. The culture medium was switched to Neurobasal medium (Life
135 Technologies) containing N21, 2 mM L-glutamine (Life Technologies), and 1 µM K03861 when the cells

136 were plated. Cultures were maintained in the medium for 7 days, and the medium was changed every
137 other day before cells were harvested for immunostaining or CUT&Tag.
138
139 **CUT&Tag**
140 Cells from proliferating iMOPs and iMOP-derived neurons were harvested for and processed using the
141 CUT&Tag-IT Assay Kit (Active Motif) described by the manufacturer. Cells were gently dissociated using
142 TrpLE Express (Life Technologies), counted and collected by centrifugation. For each CUT&Tag reaction,
143 500,000 cells were used. The supernatant from the cell pellet was removed, and cells were resuspended
144 in wash buffer and placed on ice. Cells were enriched using magnetic Concanavalin A beads and
145 resuspended in an antibody buffer containing a primary antibody to the protein of interest. Antibodies for
146 H3K4me3 (Active Motif), p300 (Developmental Studies Hybridoma Bank), CHD4 (Abcam) and IgG
147 (Jackson Immunochemicals) were used for individual samples. All antibodies are listed in Table 2. Two
148 independent samples were used for each antibody condition. Primary antibodies were incubated with the
149 cells for 2 hours at room temperature to overnight at 4°C. All antibodies for CUT&Tag were used at 1:50
150 dilution. After incubation, the cells were washed and incubated in buffer containing the assembled pA-
151 Tn5 transposomes and incubated for 1 hr at RT. Cells were washed and processed for tagmentation by
152 incubation in the appropriate buffer for 1 hr at 37°C. A solution containing EDTA, SDS and proteinase K
153 was added to stop the reaction and solubilize DNA fragments. The solution was placed on a magnetic
154 stand, and the supernatant containing soluble DNA fragments was retained. The DNA solution was
155 purified using a column. The DNA fragments were subjected to PCR amplification and purified using
156 SPRI beads. Libraries generated were quantified and subjected to quality control before performing an
157 Illumina Hiseq 3000 platform (2x150bp).
158
159 **Peak calling**
160 Paired-end CUT&Tag reads were aligned to mm10 genome assembly with bowtie2. Only mapped reads
161 were retained, written to the output, and used for the downstream analysis (Langmead and Salzberg,

162 2012). The bowtie2 SAM output files were converted into BAM files using Samtools (Li et al., 2009). After
163 alignment, sequence reads were scaled using the bamCoverage command in deepTools to remove
164 duplicates and generate normalized bigwig files with reads as Reads Per Kilobase per Million (RPKM)
165 (Ramirez et al., 2014). UCSC bigWigToBedGraph utility was used to generate bedgraph files from bigwig
166 files (Kent et al., 2010). Peaks were called using Sparse Enrichment Analysis for CUT&RUN (SEACR)
167 (Meers et al., 2019b). SEACR output bed files from CHD4, H3K4me3 and p300 were generated using
168 CHD4, H3K4me3 and p300 bedgraph files as target files while using IgG bedgraph file as a threshold.
169 BEDtools (Quinlan and Hall, 2010) was used to identify consensus peaks with at least 10% reciprocal
170 overlap between replicate samples. Only consensus peaks were used for downstream analysis.
171 CUT&Tag signal tracks were visualized on Integrative Genomic Viewer (IGV) (Robinson et al., 2011).
172

173 **Identifying CHD4-bound promoters and enhancers**

174 To perform a global survey of CHD4-bound promoters and enhancers, we first defined CHD4-bound
175 promoters and enhancers in proliferating iMOPs and iMOP-derived neurons. H3K4me3 and p300 were
176 used as promoter and enhancer marks, respectively. CHD4 bound promoters (CHD4+ H3K4me3+) and
177 enhancers (CHD4+ p300+) in iMOPs were identified using bedtools intersect command. CHD4+
178 H3K4me3+ were identified as regions with at least one base pair overlap between CHD4 and H3K4me3
179 peaks. CHD4+ p300+ regions were defined using the same strategy using CHD4 and p300 peaks.
180 SEACR total signals were obtained from the SEACR output file and plotted as box and whisker plots to
181 show the quartiles, mean (circle) and median (line) values. Cell state-specific CHD4-bound promoters or
182 enhancers were identified based on their presence or absence in progenitors and neurons. Genome
183 arithmetic was done using bedtools.
184

185 **Heatmap and profile plots**

186 Heatmaps and profile plots were generated using deepTools. The signal and region files were obtained
187 from CUT&Tag data. Normalized bigwig files from two replicates were merged using bigwigCompare to

188 acquire average bigwig files and used as signal files. The summit regions corresponding to the maximum
189 SEACR peak signal from CHD4 were used as region files. To visualize CHD4 and H3K4me3 reads as
190 heatmaps or profile plots, deepTools were used. Plots were centered at summits of CHD4+ H3K4me3+,
191 and the average CHD4 or H3K4me3 bigwig signals were plotted +/- 3 kb from the summits. To visualize
192 CHD4 and p300 reads, the summits from CHD4+ p300+ were used as the center, and the average bigwig
193 signals of either CHD4 or p300 bigwig files were plotted within +/- 3kb of the summits.
194
195 **Quantification of heatmap total signals**
196 To quantify CUT&Tag signals displayed in heatmaps, deepTools the --outFileNameMatrix option was
197 used to retrieve the matrix of signal values underlying the heatmaps. CUT&Tag signals within specified
198 genomic regions were added to obtain the summed signal values. Heatmap signals between progenitors
199 and neurons within the +/- 3kb window were visualized as box and whisker plots.
200
201 **Gene ontology (GO) analysis**
202 To annotate CHD4+ common and neuron-specific promoters and enhancers, ChIPpeakAnno was utilized
203 to determine the closest genes along with the corresponding ensembl gene IDs to those regions (Zhu et
204 al., 2010). Unique ensembl gene IDs near CHD4-bound promoters and enhancers were used for GO
205 analysis using DAVID (The Database for Annotation, Visualization and Integrated Discovery) (Huang et
206 al., 2009).
207
208 **Statistical analysis**
209 Statistical analyses were performed using either R or OriginPro (Origin Lab) for normally distributed data.
210 The means of data were presented and subjected to an unpaired two-tailed Student's t-test to determine
211 statistical significance and provide a p value. Results with p values <0.05 were considered statistically
212 significant. Unless noted, the p values are defined as $*p<0.05$, $**p<0.01$, and $***p<0.001$. Bar graphs

213 display the means ± standard error of the mean (SEM), and violin plots show the distribution and mean
214 of the data points.
215
216 Data for CUT&Tag and RNAscope were determined not to be normally distributed using the Shapiro-
217 Wilks normality test. The median was presented and subjected to a non-parametric Wilcoxon rank-sum
218 test to determine whether the paired samples differed statistically. Analysis of the data was performed in
219 R. The normalized read counts (RPKM) from CUT&Tag were displayed as box and whisker plots to show
220 the quartiles, means and medians. Horizontal lines within the box denoted the median values, while the
221 circles represented the means. The number displayed in the text indicates the median ± standard
222 deviation of CUT&Tag signals for box and whisker plots. The RNAscope images were counted to
223 determine the distribution, mean and median of puncta counts per cell. Unless noted, the p values from
224 the Wilcoxon rank-sum test were defined as $p < 0.0001$ to be significant. The variance was calculated as
225 the sum of the squared difference between puncta counts and the sample mean and divided by the
226 sample size minus one. The Levene test for the homogeneity of variance was used to determine whether
227 the variances were statistically significant. The p values from the Levene test were defined as $p<0.05$ to
228 be significant.
229

230 **Results**

231

232 **CHD4 expression in cochlear cell types**

233

234 SGNs are bipolar and pseudounipolar neurons of the cochlea. The soma of SGNs reside within the
235 modiolus and extends a peripheral process through Rosenthal's canal towards the sensory hair cells,
236 while a central process from the cell soma projects to the cochlear nucleus in the brainstem. SGNs are
237 broadly classified as type I and type II neurons. Type I SGNs are the primary afferents that consist of 90-
238 95% of the neuronal population in the spiral ganglion. Type I SGNs are myelinated and form a single
239 synaptic bouton with inner hair cells that reside in the organ of Corti (Fig. 1A). Multiple type I SGNs
240 synapse along the basolateral surface of inner hair cells (IHCs) (Liberman, 1982). Type I SGNs differ in
241 sensitivity to sound and spontaneous firing rate (SR), as revealed by single-fiber recordings in the cat
242 auditory nerve (Kiang et al., 1965). The relationship between threshold and SR predicted three distinct
243 populations of low, medium and high SR neurons (Liberman, 1978). These three subtypes are present
244 irrespective of tonotopic position along the length of the cochlea (Borg et al., 1988; el Barbary, 1991;
245 Schmiedt, 1989; Shrestha et al., 2018; Sun et al., 2022; Taberner and Liberman, 2005; Winter et al.,
246 1990). SGNs display different receptors and ion channel regulators that shape their sensitivity and SR.
247 The molecular heterogeneity has been correlated to the differences in electrophysiological properties of
248 these neurons (Adamson et al., 2002; Chen et al., 2011; Liu et al., 2014; Liu and Davis, 2014).

249

250 Type II afferent neurons account for 5–10% of the neuronal population (Ruggero et al., 1982; Spoendlin,
251 1972). Type II SGNs are pseudounipolar and unmyelinated neurons that turn towards the cochlear base
252 (Zhang and Coate, 2017). During outgrowth, Type II SGN peripheral axons turn after the growth cone
253 passes between the basolateral surfaces of the inner pillar cells. Turning occurs among the outer pillar
254 and Deiters' cells as they are directed towards the cochlear base (Fig. 1A). This process is mediated by
255 planar cell polarity complexes formed between cochlear-supporting cells for non-cell autonomous

256 regulation of axon pathfinding (Ghimire and Deans, 2019; Ghimire et al., 2018). The peripheral axons
257 then gradually ascend apically toward the outer hair cells (OHCs) after turning to join other type II axons
258 in one of three outer spiral bundles that extend along the length of the cochlea (Fig. 1B). Each type II
259 afferent neuron innervates multiple OHCs from the same row, with individual OHC receiving an *en-*
260 *passant* contact from a type II afferent neuron (Zhang and Coate, 2017).
261
262 To determine the expression of CHD4, neonatal cochleae from embryonic (E)18.5 embryos were
263 harvested. At this point, type I and type II SGNs are morphologically distinct, and the neurites have
264 extended toward IHCs and OHCs, respectively. The cochleae were subjected to immunostaining with
265 CHD4 and TUBB3 antibodies to mark the presence of type I and type II SGNs along with CHD4 (Fig.
266 1C). The fiber tracks from their innervation pattern can identify the type of SGNs. As previously described,
267 many different cell types within the organ of Corti, including IHCs and OHCs, express CHD4 (Layman et
268 al., 2013). We confirmed the presence of CHD4 in MYO7A labeled hair cells (Fig. 1D). CHD4 was also
269 expressed in the nuclei of inner pillar, outer pillar and the three rows of Dieter cells and other supporting
270 cells (Fig. 1E). Finally, CHD4 was strongly expressed in the nucleus of spiral ganglion neurons (SGNs)
271 marked by TUBB3 in the modiolus (Fig. 1F). Expression of CHD4 was present in all TUBB3-marked
272 SGNs. The presence of *Chd4* transcripts in developing SGNs (Lu et al., 2011) and our results suggest
273 that CHD4 may function in SGNs during inner ear development.
274
275 **Deletion of *Chd4* in SGNs**
276
277 CHD4 is present in many inner ear cell types, and mutations that inactivate CHD4 chromatin remodeling
278 activity may contribute to improper development or dysfunction of multiple inner ear cell types. Since
279 SGNs were highly expressed CHD4, we wanted to delineate how CHD4 ablation in SGNs contributes to
280 the development of the cochlea and hearing loss. Targeted ablation of CHD4 from SGNs using a
281 Neurogenin1 (Ngn1) CreER^{T2} *Chd4*$^{flox/flox}$ animal was accomplished. The Ngn1 CreER^{T2} *Chd4*$^{flox/flox}$

282 animals contain two copies of the *Chd4* conditional knockout (cKO) allele where loxP sites flanked exons
283 that code for the ATPase domain required for nucleosome repositioning (Williams et al., 2004). The Ngn1
284 CreER^{T2} transgenes harbor a tamoxifen-inducible Cre expressed in neurosensory progenitors and can
285 be used for genetic manipulations in SGNs (Koundakjian et al., 2007). Tamoxifen administration to Ngn1
286 CreER^{T2} animals allowed Cre-mediated excision of loxP-flanked DNA in inner ear neurosensory
287 progenitors that become SGNs (Koundakjian et al., 2007; Raft et al., 2007). To ensure Cre activity was
288 present in the intended cell types, *Chd4*$^{flox/flox}$ Ngn1 CreER^{T2} were crossed to the Ai9 tdTomato reporter
289 (Madisen et al., 2010). In the triple transgenic animals, tamoxifen administration allows Cre-activated Ai9
290 tdTomato reporter expression and enables fluorescence visualization of SGN cell bodies and axonal
291 projections while simultaneously deleting *Chd4* (Fig. 2A). Control (Ngn1 CreER^{T2}; Ai9) and *Chd4* cKO
292 (Ngn1 CreER^{T2}; *Chd4*$^{flox/flox}$; Ai9) lines were generated. Timed matings from either control or *Chd4* cKO
293 lines produced pregnant dams were administered with tamoxifen to produce embryos for analysis.
294
295 During inner ear development, delaminating otic progenitors around embryonic day (E)9 from the
296 proneurosensory domain of the otic vesicle coalesce to form the cochlear-vestibular ganglion (CVG). As
297 development progresses, the CVG neurons segregate to create the spiral ganglion. A population of
298 neurons exits the cell cycle and terminally differentiates at the base and middle of the cochlea starting
299 from E9.5-10.5. Most SGNs exit the cell cycle around E11.5 in the middle and base of the cochlea, while
300 cells in the apex exit the cell cycle at E12.5. After exiting the cell cycle, peripheral projections from SGNs
301 extend toward the sensory epithelium of the cochlea. At E12.5, SGN projections begin to extend beyond
302 the spiral ganglion border. At E15.5, SGN peripheral axon outgrowth continues along the length of the
303 cochlea. Type I SGNs form radial fiber bundles that undergo fasciculation. Between E15.5-18.5, type I-
304 like SGN processes show extensive branching around and beyond the inner hair cells. The neurites are
305 subsequently refined by retracting from the outer hair cell region (Appler and Goodrich, 2011; Coate et
306 al., 2015). Type II SGNs are notably distinct from Type I SGNs by E16.5 based on their peripheral
307 projections ending at the outer hair cell region (Bruce et al., 1997). The Ngn1 CreER^{T2} animals with a

308 reporter can mark delaminating neurosensory progenitors that develop into type I and type II SGNs at
309 the aforementioned developmental stages (Koundakjian et al., 2007).
310
311 *Chd4* was deleted by administering daily tamoxifen doses to pregnant dams between E8.5-10.5. During
312 this time, *Chd4* was deleted from neurosensory progenitors that give rise to SGNs. Labeled cells were
313 used to study the consequences of *Chd4* ablation in the development of type I and type II SGNs. E18.5
314 embryos were harvested from pregnant dams after tamoxifen treatment. Although some embryos
315 survived, many resorptions occurred perinatally after tamoxifen administration. Quantification and
316 comparison of resorbed embryos from control and *Chd4* cKO dams suggest a significant reduction in
317 viability of *Chd4* cKO embryos (Fig. S1A). Quantifying the number of surviving embryos from individual
318 litters obtained from pregnant dams showed a statistically significant reduction in embryo viability after
319 *Chd4* deletion (Fig. S1B). Cre recombinase expression in the Ngn1 CreERT^2 is not limited to the inner
320 ear but can also be observed throughout the central nervous system (Kim et al., 2011). These findings
321 suggest that deleting *Chd4* in other cell types may decrease viability in the *Chd4* cKO embryos.
322
323 From the remaining embryos, cochleae were harvested and used for immunostaining. To ensure that
324 genetic deletion of *Chd4* lacked protein, immunofluorescence labeling of the CHD4 protein was done.
325 TUBB3 immunofluorescence was used to identify SGNs. The tdTomato fluorescence suggested Cre
326 activity was present in TUBB3 marked SGNs in both control and *Chd4* cKO cochleae samples. Even
327 though SGNs were present in the cochleae, only the CHD4 signal was seen in controls and not *Chd4*
328 cKO cochleae (Fig. 2B). These results showed that CHD4 protein was absent in the *Chd4* cKO cochlea
329 after tamoxifen treatment and that CHD4 was not essential for SGN viability at embryonic and neonatal
330 stages. In E18.5 embryonic cochlea, an increase in the number of tdTomato+ and TUBB3-negative cells
331 was observed in *Chd4* cKO (Fig. 2C). To quantify the percentage of the marked cell populations, SGNs
332 from dissected cochlea were divided into three regions corresponding to the apex, middle and base of
333 the cochleae. In controls, a low percentage of cells lacking TUBB3 but expressing tdTomato was

334 observed (apex: 6.81 ± 1.69%, middle: 4.07 ± 1.94%, base: 3.95 ± 1.74%), while in *Chd4* cKO cochlea,
335 increased percentages of these cells were observed along the length of the cochleae (apex: 12.06 ±
336 2.25%, middle: 8.73 ± 0.91%, base: 7.82 ± 1.29%; apex, $p<0.136$, middle, $p<0.095$; base, $p<0.148$) (Fig.
337 2D). The percentage of TUBB3 labeled SGNs marked by tdTomato allowed us to confirm the efficiency
338 of Cre-mediated activity in these cells. In control embryos, Cre activity was observed in almost all SGNs
339 with a slight decrease in labeled cells at the apex (apex: 89.86 ± 3.56%, middle: 97.09 ± 1.48%, base:
340 98.97 ± 0.36%). Since development proceeds in a base-to-apex manner, the decreased percentage of
341 tdTomato-marked cells located at the apical region of the cochlea was likely due to a small population of
342 late-born neurons that was not exposed to tamoxifen during the time window of administration. *Chd4* cKO
343 displayed similar percentages of tdTomato marked cells (apex: 84.35 ± 2.99%, middle: 95.71 ± 1.96%,
344 base: 98.91 ± 0.2%; apex $p<0.302$; middle $p<0.603$; base, $p<0.9$). The percentages of
345 tdTomato+TUBB3+ cells from control and *Chd4* cKO cochlea were not statistically different (Fig. 2E).
346 The numbers of tdTomato+ cells from *Chd4* cKO were not significantly different from control (44.22 ±
347 0.41% for control, 49.7 ± 2.32% for *Chd4* cKO, $p<0.081$) (Fig. 2F). These results suggest that tamoxifen-
348 induced Cre recombination was efficient along the entire length of the cochlea and was similar between
349 control and *Chd4* cKO cochleae.
350
351 ***Chd4* cKO cochleae displayed altered fasciculation of radial fiber bundles**
352
353 Deletion of *Chd4* in embryos showed that SGNs were present and in comparable percentages as
354 controls. Although *Chd4* may not dramatically affect the viability or early developmental stages, we
355 wanted to determine whether loss of *Chd4* showed discernable differences at later stages. Post-mitotic
356 neurons from the spiral ganglion extend neurites towards inner and outer hair cells, starting from the base
357 to the apex. Type I and type II SGNs target IHCs and OHCs, respectively. Type I and type II SGN fiber
358 tracks and innervation patterns were marked by performing whole mount TUBB3 immunostaining using
359 cochleae from control and *Chd4* cKO (Fig 3A).

360

361 The peripheral axons of type I SGNs extend from the soma to form a radial bundle. The type I SGN fibers
362 fasciculate, the terminals extensively branch around the inner spiral plexus (ISP) and retract from the
363 outer hair cell region back into the IHC region (Fig 3B). In *Chd4* cKO cochleae, radial fibers were less
364 compact and showed wider nerve fascicles. The area between the fiber bundles was identified by
365 converting TUBB3 immunofluorescent images to black-and-white binary images. The white regions
366 between fiber bundles and the total area from the SGN soma to the sensory epithelium were determined
367 from images taken along the length of the cochlea (Fig. 3C). The percent area unoccupied by radial fibers
368 relative to the total area was calculated, and used as a metric for fasciculation (Fig. 3D). The average
369 percentage of unoccupied space in *Chd4* cKO cochleae was significantly decreased (33.19 ± 2.59% for
370 control and 25.12 ± 1.28% for *Chd4* cKO, $p<0.049$). The result suggested that the radial fibers from *Chd4*
371 cKO cochleae covered more area and thus were wider than controls (Fig. 3E). The fiber bundles were
372 counted in control and *Chd4* cKO cochleae to determine the fascicle numbers in the inner spiral plexus
373 (ISP), (Fig. 3F). The ISP consists of the region where radial fibers extend from the soma through
374 the *habenula perforata* to innervate the IHC (Fig. 1). The average number of fascicles in ISP per inner
375 radial bundle increased significantly in *Chd4* cKO cochleae (4.48 ± 0.16 bundles for control and 6.54 ±
376 0.67 bundles for *Chd4* cKO, $p<0.0083$) (Fig. 3G). These results show an increased number of inner radial
377 fiber bundles and less compact bundling of the nerve fiber.

378

379 ***Chd4* cKO cochleae display improper turning of type II fibers**

380

381 Type II SGNs constitute only 5-10% of the total SGN population, but their axonal projections are spatially
382 distinct from type I SGNs. During development, their peripheral processes cross the tunnel of Corti into
383 the outer hair cell region, where the axons make a right-angle turn and travel from the base of the cochlea
384 towards the apex to make *en passant* synapses with outer hair cells. The outer spiral fibers are the
385 bundled neurites from type II SGNs that extend along the OHC region. Each OHC is innervated by 2-5

386 type II SGNs (Huang et al., 2012; Martinez-Monedero et al., 2016). To look at the outer spiral fiber tracks,
387 TUBB3 labeled neurons from whole mount cochleae were used for analysis (Fig. 4A). The magnified
388 images of outer spiral fibers usually display three main fiber tracks that travel along individual rows of
389 outer hair cells with intermittent fibers crossing these tracks. To show quantitative differences between
390 the outer spiral tracks, intensity profiles from control and *Chd4* cKO cochleae images spanning the outer
391 hair cell region were taken (Fig. 4B). Measurements of the intensity profile show different peaks
392 corresponding to the presence of fibers. The intensity profile plot showed three prominent peaks in the
393 control cochlea (black). In contrast, Chd4 cKO cochlea (red) displayed additional peaks (Fig. 4C). The
394 data suggested that there are type II SGN fibers or individual axons that detract from the outer fiber tracts
395 (Fig. 4C). Each major peak corresponds to an outer spiral bundle consisting of multiple fibers. The
396 appearance of the minor peaks within a major peak corresponds to the increased dispersion of the fibers
397 within an outer spiral fiber. The number of distinct fibers observed by fluorescent microscopy in the outer
398 hair cell region was counted and normalized based on the area to validate the altered axon paths. Similar
399 to the intensity profile, the number of fibers in the OHC area increased in *Chd4* cKO samples compared
400 to controls (13.98 ± 0.73 fibers for control and 17.64 ± 0.78 fibers for *Chd4* cKO, $p<0.027$) (Fig. 4D).
401 These results suggest aberrant bundling of the outer spiral fibers after *Chd4* ablation in SGNs.
402
403 We also noticed the aberrant turning of the outer spiral fiber tracks. Turning of the type II SGN fibers
404 usually occurs near the inner pillar cell (IPC), outer pillar cell (OPC) or Dieter cell (DC) region. Confocal
405 micrographs were acquired below the outer hair cell layer up to the sensory epithelium to visualize the
406 fiber turning. Individual fibers from control cochleae turned towards the base of the cochlea before joining
407 one of the three outer spiral fiber tracks. In contrast, the *Chd4* cKO cochleae showed fibers turning in the
408 opposite direction (Fig. 4E, yellow arrows). Incorrectly turned type II fibers were quantified in control and
409 Chd4 cKO cochleae (Fig 4F). These data showed that the deletion of *Chd4* increases the incorrect turning
410 of type II SGNs in the outer spiral fibers (0.12 ± 0.06 fibers for control and 1.93 ± 0.14 fibers for *Chd4*
411 cKO, $p<0.00028$. Turning of the fibers has previously been shown to require cell signals from supporting

412 cells (Deans, 2022; Ghimire and Deans, 2019; Ghimire et al., 2018). To ensure that supporting cells in
413 the organ of Corti were present and not indirectly affected by *Chd4* deletion, immunostaining for both hair
414 cells using MYO7A and supporting cells SOX2 was performed in control and Chd4 cKO cochlea. A single
415 row of inner hair cells and three rows of outer hair cells were present in both samples. Moreover, SOX2-
416 labeled supporting cells showed the presence of organized supporting cells residing below hair cells (Fig.
417 S2). These results suggest that *Chd4* deletion in SGNs affects the turning of type II SGNs in a cell-
418 autonomous manner.
419
420 **_Chd4_ cKO cochleae display aberrant basal to apical axon path towards outer hair cells**
421
422 Alterations in axon paths could also be due to how fibers exit Rosenthal's canal and ascend toward the
423 outer hair cells. To determine if this is the case, reconstructed confocal images of MYO7A-labeled hair
424 cells provide a landmark for the terminal destination of axons. We observed that many type II tracks take
425 a more circuitous route toward the OHCs because the fibers initially descend basally and migrate further
426 away from the soma of outer hair cells (Fig. 4G). The distances were obtained from the bottom of
427 individual OHC somas to the furthest detectable axon fibers directly below. The measurements were
428 used to quantify the aberrant axon path (Figure 4H). The measurements showed an increase in the
429 average distance of the fibers to the bottom of hair cells in *Chd4* cKO cochleae (17.84 ± 0.66μm for
430 control and 29.87 ± 3.74μm for *Chd4* cKO, $p<0.034$). The increased distance measured in *Chd4* cKO
431 cochleae suggested that outer spiral fibers do not properly ascend from Rosenthal's canal towards the
432 outer hair cells (Fig. 4I). Many of these changes in fiber tracks and innervation patterns observed both in
433 type I and type II SGNs are reminiscent of axon guidance defects. Although these findings implicate
434 CHD4 in axon pathfinding, the molecular targets for CHD4 in SGNs are unknown.
435
436 **Enrichment of CHD4 at cis-regulatory regions of _Eph_ and _Ephrin_ genes**
437

438 CHD4 function is cell-type dependent, and its chromatin activity likely alters a unique repertoire of cis-
439 regulatory elements in SGNs to control gene expression. A significant hurdle is identifying high-
440 confidence occupancy sites for CHD4 in SGNs by chromatin immunoprecipitation followed by deep
441 sequencing (ChIP-seq) or Cleavage Under Targets & Tagmentation (CUT&Tag). The inability to identify
442 these high-confidence sites in SGNs is partly due to the large number of cells required for the
443 experiments. Instead of primary SGNs, we used immortalized multipotent otic progenitor (iMOP)-derived
444 neurons to determine genome-wide binding sites for CHD4 to identify potential target genes.
445 Immortalized multipotent otic progenitors (iMOP) derived neurons are highly similar at the transcriptome
446 level to primary otic progenitors from which they were derived and can differentiate into cells that display
447 bipolar and pseudounipolar morphology similar to SGNs (Kwan et al., 2015).
448
449 Immunostaining confirmed the presence of CHD4 in the nucleus of proliferating iMOPs and TUBB3-
450 expressing iMOP-derived neurons (Fig. 5A). To identify genome-wide CHD4 binding sites, CUT&Tag
451 was performed using CHD4 antibodies on proliferating iMOP and iMOP-derived neurons. CHD4
452 occupancy is cell-type specific and are recruited to active promoters and enhancers to repress
453 transcription (Yang et al., 2016; Yoshida et al., 2019). We used the H3K4me3 and p300 marks as
454 genomic landmarks for promoters and enhancers. Sparse Enrichment Analysis for CUT&RUN (SEACR)
455 identified regions of high-confidence enrichment, known as peaks, from all CUT&Tag sequence reads
456 (Meers et al., 2019a). We compared CHD4 peaks to H3K4me3 and p300 bound regions. The heatmaps
457 provided a distribution of the reads within a +/- 3 kb window. The profile plots allowed us to evaluate the
458 read density over the same genomic regions qualitatively. We identified CHD4+ H3K4me3+ regions
459 based on the occupancy of CHD4 and H3K4me3 peaks in proliferating iMOP cells and iMOP-derived
460 neurons (Fig. S3B). The CHD4+ H3K4me3+ regions corresponded to CHD4-bound promoters. Similarly,
461 we defined CHD4+ p300+ regions in proliferating iMOP cells and iMOP-derived neurons (Fig. S3C). The
462 CHD4+ p300+ regions corresponded to CHD4-bound enhancers. From the profile plots, we noticed that
463 the CHD4 signal increased in iMOP-derived neurons compared to proliferating iMOPs at both promoters

464 and enhancers. We quantified and compared the CHD4 total signals at CHD4+ H3K4me3+ promoters
465 and CHD4+ p300+ enhancers between proliferating iMOP and iMOP-derived neurons. We showed that
466 at CHD4-bound promoters, CHD4 total signals increased 2.80 fold in iMOP-derived neurons (57,811.40
467 ± 65,983.40 RPKM) compared to proliferating iMOPs (20,684.90 ± 25,408.89 RPKM, $p<2.2 \times 10^{-16}$). At
468 CHD4-bound enhancers, we found a 4.65 fold increase of CHD4 total signals in iMOP-derived neurons
469 (134,027.50 ± 102,349.97 RPKM) compared to proliferating iMOPs (28,837.65 ± 29,014.11 RPKM, $p<2.2$
470 $\times 10^{-16}$) (Fig. 5B). The results suggest that increased enrichment of CHD4 at cis-regulatory regions in
471 iMOP-derived may regulate gene expression during neuronal differentiation.
472
473 To investigate the involvement of CHD4 during neuronal differentiation, we identified CHD4 binding sites
474 present in iMOP-derived neurons. We did this by comparing CHD4-bound regions between proliferating
475 iMOPs and iMOP-derived neurons. At CHD4+ H3K4me3+ promoters, we found 982 progenitor-specific,
476 168 neuron-specific, and 1,092 common promoters in both proliferating iMOPs and iMOP-derived
477 neurons. At CHD4+ p300+ enhancers, we identified 2,106 progenitor-specific, 223 neuron-specific, and
478 750 common enhancers (Fig. 5C). We focused on common and neuron-specific regions since CHD4
479 activity may exert epigenetic changes at these sites during neuronal differentiation. We generated
480 heatmaps and profile plots for each of the regions. At common promoters, we observed a 1.20-fold
481 increase of H3K4me3 in iMOP-derived neurons (25,871.92 ± 12,797.1 RPKM) compared to proliferating
482 iMOPs (21,550.36 ± 9,015.1 RPKM, $p<3.67 \times 10^{-23}$) and a 2.28-fold increase in CHD4 in iMOP-derived
483 neurons (5,407.49 ± 2,955.04 RPKM) compared to proliferating iMOPs (2,371.49 ± 1573.27 RPKM,
484 $p<3.46 \times 10^{-282}$). At neuron-specific promoters, a 1.3 fold increase in H3K4me3 (proliferating iMOP
485 17,105.85 ± 10,709.21 RPKM, iMOP-derived neurons 22,411.04 ± 14,180.57 RPKM, $p<3.87 \times 10^{-7}$) and
486 3.30 increase in CHD4 (proliferating iMOP 1,397.09 ± 2,617.01 RPKM, iMOP-derived neuron 4,608.37 ±
487 3,173.27 RPKM, $p<4.22 \times 10^{-45}$) was observed in iMOP-derived neurons (Fig. 5D). All observed increase
488 in H3K4me3 and CHD4 were statistically significant.
489

490 We performed a similar analysis for enhancers. The heatmaps and profile plots showed a distribution of
491 p300 and CHD4 centered at common and neuron-specific enhancers. A 3.37-fold increase in p300
492 (proliferating iMOP = 2,838.41 ± 1,713.93 RPKM, iMOP-derived neuron = 9,578.39 ± 4531.32 RPKM,
493 $p<5.92 \times 10^{-223}$) was observed at common enhancers. CHD4 displayed a 2.84-fold increase in signal from
494 iMOP-derived neurons (proliferating iMOP 4,068.79 ± 2,542.82 RPKM, iMOP-derived neuron 11,559.34
495 ± 4,647.43 RPKM, $p<9.30 \times 10^{-210}$). At common and neuron-specific enhancers, a statistically significant
496 increase in signal was detected for p300 and CHD4 in iMOP-derived neurons compared to proliferating
497 iMOPs (Fig. 5E). These results suggest that CHD4 was significantly enriched at specific promoters and
498 enhancers during neuronal differentiation. The increased occupancy likely alters the chromatin state of
499 these cis-regulatory regions to modulate transcription.
500
501 To gain biological insights into CHD4 targets, genes near the common and neuron-specific regulatory
502 elements were identified (Table S1). The identified target genes were used for gene ontology analysis.
503 Gene ontology (GO) analysis revealed function in chromatin organization ($p< 5.1 \times 10^{-14}$), which is
504 consistent with the predicted cellular process of CHD4 in inner ear neurons. Other biological processes
505 such as ephrin receptor signaling ($p< 4.9 \times 10^{-5}$), axon guidance ($p< 2 \times 10^{-13}$), semaphorin-plexin signaling
506 during axon guidance ($p< 2.7 \times 10^{-2}$), axonal fasciculation ($p< 1.6 \times 10^{-2}$), and axonogenesis ($p<1.6 \times 10^{-14}$)
507 were some of the notable cellular processes (Fig. S3A). The GO analysis suggested that CHD4 gene
508 targets may regulate processes involved in axon pathfinding, including ephrin receptor signaling. We
509 identified *Epha4*, *Epha7*, *Ephb3*, *Efna3*, *Efna4*, *Efnb2*, *Efna5*, *Efnb1*, and *Ephb2* as candidate genes
510 involved in ephrin receptor signaling based on their proximity to CHD4-bound promoter and enhancer
511 regions (Table S1). Ephrin signaling pathways are essential in guiding SGN peripheral axons. We
512 focused on *Epha4*, *Epha7*, and *Efnb2* because these genes have previously been implicated to function
513 in the inner ear (Coate et al., 2012; Defourny et al., 2013; Kim et al., 2016; Petitpre et al., 2018; Sanders
514 and Kelley, 2022). At *Epha4* and *Epha7*, CHD4 and H3K4me3 peaks were observed near the
515 transcriptional start site. We also observed an increase in CHD4 and p300 in iMOP-derived neurons at

516 multiple intronic regions, a region upstream at *Epha4* and a singular downstream site at *Epha7* (Fig. 5F).
517 A similar observation was noted for *Efnb2* (Fig. S3D), where CHD4 was enriched at the H3K4me3 marked
518 promoter along with increased CHD4 and p300 signals at a downstream enhancer region. These results
519 implicate that CHD4 binding to promoters and enhancers may control the transcription of ephrin receptors
520 and ligands. The altered expression of these genes may be pertinent to the axon guidance deficits seen
521 in the *Chd4* cKO cochleae.
522
523 **Chd4 cKO showed increased *Epha4* mRNA levels in SGNs**
524
525 To test if deletion of CHD4 in SGNs affects the level of ephrin molecules, cochleae from control and *Chd4*
526 cKO were subjected to RNAscope fluorescence *in situ* hybridization. We used *Epha4*, as an example of
527 how transcription is affected after CHD4 ablation. *Calbindin2* (*Calb2)* transcripts were used as a marker
528 for SGNs. TUBB3 immunolabeling was combined with RNAscope to demarcate individual cells for
529 quantification (Fig. 6A). The number of counted punctas from RNAscope measured the relative number
530 of mRNA molecules. *Calb2* and *Epha4* puncta were counted from individual TUBB3 marked SGNs. The
531 average number of *Epha4* puncta in the SGN population increased significantly in *Chd4* cKO (13 ± 6.29
532 *Epha4* puncta/cell) compared to control (7 ± 4 *Epha4* puncta/cell, $p<2.2 \times 10^{-16}$) and was statistically
533 significant. Concurrently, there was no significant difference observed in *Calb2* transcript levels between
534 *Chd4* cKO (8 ± 5.51 Calb2 puncta/cell) and control (9 ± 6.16 *Calb2* puncta/cell, $p<0.13$) (Fig. 6B). The
535 distribution of puncta counts per cell was visualized by plotting the *Calb2* and *Epha4* puncta counts
536 separately (Fig. 6C) In addition to the increase in puncta counts for each cell in *Chd4* cKO SGNs, we
537 noted an increased variance of *Epha4* counts per cell. The variance provides the spread of puncta per
538 cell around the median. Each histogram was converted to a kernel density estimate to describe the
539 distribution probability of puncta in cells. A 2.47-fold increase in the variance of *Epha4* transcripts was
540 observed in *Chd4* cKO ($\sigma^2 = 39.5$) compared to control SGNs ($\sigma^2 = 15.99$, $p<2.27 \times 10^{-14}$). The non-
541 overlapping regions in the kernel density estimates reflect the increased probability of observing cells

542 with higher *Epha4* transcript levels in the absence of *Chd4* (Fig. 6D). In contrast, the variance of *Calb2*
543 transcripts showed a 1.25-fold decrease in *Chd4* cKO (σ^2 = 30.36) compared to the control (σ^2 = 37.93,
544 p <0.035). Although the variance for *Calb2* is significant, we did not observe CHD4 or the H3K4me3 mark
545 at the *Calb2* promoter (Fig. S3E). The enrichment pattern at *Calb2* was distinct from *Epha4*, *Epha7,* and
546 *Efnb2*, suggesting an indirect effect of *Chd4* deletion or a different mechanism causing the decreased
547 variance. The results suggest that the increased likelihood of *Chd4* cKO SGNs to harbor more *Epha4*
548 transcripts is likely due to the loss of transcriptional repression. The data indicate that CHD4 normally
549 fine-tunes transcription in SGNs during development, and ablation of *Chd4* increases transcript levels of
550 axon guidance genes, resulting in aberrant peripheral axon pathfinding.
551
552 **Discussion**
553
554 *De novo* pathogenic variants of *CHD4* correlate to SIHIWES, an autosomal dominant
555 neurodevelopmental disorder**.** Patients with pathogenic variants of CHD4 show variable symptoms, and
556 many display hearing loss (Sifrim et al., 2016b; Weiss et al., 2016). CHD4 is expressed in cochlear
557 supporting cells and hair cells from E18 to P21 (Layman et al., 2013). Gene expression analysis showed
558 that CHD4 transcripts are present and changing in developing murine SGNs from E12 to P15 (Lu et al.,
559 2011). CHD4 has a core ATPase SWI/SNF domain that hydrolyzes ATP and converts it into chromatin
560 repositioning activity. Some pathogenic mutations result in a CHD4 protein with reduced chromatin
561 remodeling activity (Weiss et al., 2020). To clarify the contribution of CHD4 in SGNs, we employed a
562 conditional knockout mouse model that allows Cre-dependent inducible deletion of the exons coding for
563 the ATPase domain of CHD4 in SGNs. The conditional knockout mouse allowed us to separate the CHD4
564 function from other inner ear cell types, such as hair cells and supporting cells. Our current results
565 implicate a cell-autonomous role for CHD4 in the pathfinding of SGN peripheral axons during inner ear
566 development. The lack of CHD4 chromatin remodeling activity in SGNs may result in aberrant axon
567 guidance. The altered pathfinding may affect the transmission of neural signals and innervation of hair

568 cells. These deficits likely contribute to hearing loss in patients with SIHIWES and provide insight into
569 how other neural circuits may be affected.
570
571 CHD4 is a core subunit in the Nucleosome Remodeling and Deacetylase (NuRD) complex (Tong et al.,
572 1998; Xue et al., 1998; Zhang et al., 1998). The NuRD complex acts mainly as a transcriptional repressor
573 and localizes to sites of active transcription. At these sites, CHD4 repositions nucleosomes and subunits
574 of the complex, such as histone deacetylases (HDAC) 1 and 2 deacetylate histones (Morra et al., 2012;
575 Watson et al., 2012). Although CHD4 has many other paralogs, distinct NuRD complexes with individual
576 CHD paralogs (CHD3, CHD4, and CHD5) have specific molecular functions and do not compensate for
577 the loss of a singular CHD. The remaining paralogous CHDs did not compensate for the cellular effects
578 of ablating CHD4 (Nitarska et al., 2016). CHD4-containing NuRD complexes in the inner ear may contain
579 distinct protein subunits that alter the epigenetic landscape at cis-regulatory regions. Our results suggest
580 a role for CHD4 in axon guidance during SGN development. Even if paralogs were present in SGNs, they
581 did not fully compensate for the observed axon guidance deficits. We used iMOP-derived neurons as a
582 cellular system to show CHD4 occupancy at distinct sets of promoter and distal enhancers. During iMOP
583 neuronal differentiation, we observed increased CHD4 occupancy at these sites. We propose that CHD4
584 exerts epigenetic changes on cis-regulatory elements to attenuate transcription of axon guidance genes
585 until the appropriate developmental time. In the absence of CHD4, the core NuRD complex does not
586 form, and axon guidance genes may show increased transcription due to the absence of NuRD-
587 dependent nucleosome repositioning and histone deacetylase activities. The exquisite temporal
588 transcriptional control of axon guidance genes is likely required for appropriate fasciculation and
589 innervation patterns.
590
591 Our identified candidate set of Eph receptors and Ephrin ligands (*EphA4*, *EphA7*, and *Efnb2*) is
592 noteworthy since their functions are well-established in the developing cochlea. *Eph* receptors are a
593 family of receptor tyrosine kinases that mediate many essential processes through promiscuous

interactions with membrane-bound ephrin ligands. Ephrins are divided into the glycosyl-phosphatidylinositol (GPI) linked ephrin-A and the transmembrane ephrin-b ligands. Ephrins bind to Eph receptors of the same class, except for EphA4. EphA4 interacts with ephrin-A, B2, and B3 ligands.

Deletion of *EphA4* showed ectopic innervation of outer hair cells by a subset of type I SGNs (Defourny et al., 2013). EphA4 interacts with the ephrin-A5 ligand to control target specification, expressed primarily in OHCs and a subset of type I SGNs. Previously, *ephrin-A5* was thought to be expressed in a subset of type I SGNs, but recent evidence implicated *ephrin-A5* mainly in type II SGNs (Petitpre et al., 2018; Sanders and Kelley, 2022). The otic mesenchyme surrounding the SGN axons also expresses EphA4 (Coate et al., 2015). This pattern of EphA4 expression guides fasciculation through ephrin-B2 interactions on the developing SGN axons. Another Eph receptor, EphA7, in SGNs, is required for neurite outgrowth. Loss of *EphA7* resulted in more sparse fiber bundles and fewer synaptic contacts on inner hair cells (Kim et al., 2016). These studies implicate the function of ephrin signaling in developing peripheral auditory circuits. Although we observed axon guidance deficits in the *Chd4* cKO cochleae, the phenotypes are distinct. Using the Ngn1 CreER^{T2}, we only perturbed SGNs while leaving the other cell types, such as hair cells and otic mesenchyme, untouched. Instead of inactivating the function of ephrin receptor or ephrin ligands, *Chd4* deletion increased *Epha4* transcript levels in SGNs, revealing a molecular perturbation relevant to SIHWES disease. The *Chd4* cKO model also differs from the Eph receptor and Ephrin ligand single knockouts because it likely affects the expression of multiple axon guidance genes. The subtle cellular phenotypes in single Eph and Ephrin knockout mice suggest that the proper wiring of the peripheral auditory circuit may require the combined effects of multiple Eph and Ephrins members instead of relying on a single molecule. Our findings align with the function of numerous Eph and ephrin genes during SGN development and suggest that CHD4 may coordinate the expression of several Ephrin ligands and receptors to shape the innervation pattern of type I and II SGNs.

619 Control of gene expression plays a fundamental role in development and disease. Patients with Sifrim-
620 Hitz-Weiss disease show variable congenital disabilities. This observation is reminiscent of CHARGE
621 syndrome, a genetic disorder caused by pathogenic variants in CHD7. CHD7 and CHD4 are part of the
622 chromodomain helicase DNA-binding protein family (Micucci et al., 2015). Global chromatin regulators
623 such as CHD7 and CHD4 can robustly affect transcription and trigger cell-autonomous changes during
624 critical periods in development. We show that altering the epigenetic landscape by deleting CHD4 early
625 during otic development (E8.5-E10.5) affects pathfinding and connectivity of SGN peripheral axons at
626 multiple steps during axon guidance and may contribute to hearing loss in SIHIWES.

627 Although the phenotype is robust, penetrance is variable. We believe this is a central aspect observed in
628 mutations of chromodomain helicase DNA-binding proteins. Cellular heterogeneity may contribute to the
629 variable phenotype. There are four distinct subtypes of SGNs: type Ia, Ib, Ic and type II (Petitpre et al.,
630 2018; Shrestha et al., 2018; Sun et al., 2022). CHD4 may function differently in each neuronal subtype,
631 resulting in differing cellular phenotypes. The difference is evident in the axon guidance phenotypes
632 observed in type I compared to type II neurons. Ablation of CHD4 affected the fasciculation of radial fibers
633 and branching in the inner spiral plexus region for type I SGNs. In contrast, type II neurons displayed a
634 circuitous path to innervate the base of outer hair cells and inappropriate turning at the outer hair cell
635 region. Deleting CHD4 affected the peripheral axons differently in type I and II SGNs.
636

637 In addition to the heterogeneity of neuronal subtypes, variability within type I and II fibers was also
638 observed. The phenotypic variability includes the extent of type I radial fiber bundling and branching of
639 terminals in the inner spiral plexus. CHD4 function in SGN type Ia, b, and c fibers may contribute to the
640 observed variability. Cellular heterogeneity, however, cannot be attributed to the improper turning of
641 some type II peripheral axons. Some type II fibers are seemingly unaffected, whereas others turn in the
642 opposite direction. Stochasticity in molecular processes may be a contributing mechanism. Stochastic
643 gene expression involves biochemical processes such as transcription and translation. The limiting

644 number of molecules that catalyze transcription leads to biological variability, as observed by the dramatic
645 differences in transcript levels even within isogenic cells (Raj and van Oudenaarden, 2008). Deletion of
646 CHD4 may alter the chromatin state of cis-regulatory elements and impact the stochasticity in
647 transcription. The epigenetic perturbation could increase both transcript levels and the variance of
648 specific genes after ablating CHD4. We showed an increase in the median number of *Epha4* transcripts
649 in *Calb2* marked SGNs concomitant with an increase in the variance of the transcript numbers. The
650 increase in transcripts and variance was specific for *Epha4* and not *Calb2*. The larger variance results in
651 a broader distribution of neurons with *Epha4* and displays a cell population that exceeds the normal range
652 of *Epha4* levels in control SGNs. The percentage of neurons with increased *Epha4* transcripts may
653 possess altered EPHA4 protein expression and perturb axon guidance. In contrast, cells that retain
654 *Epha4* transcripts within the normal range retain normal axon pathfinding. The increase in transcriptional
655 variance may contribute to the heterogeneous cellular phenotypes observed for type I and type II SGNs.
656
657 We identified multiple axon guidance deficits of type I and II SGNs using a *Chd4* conditional knockout
658 mouse model. These deficits likely arise at different developmental time points and implicate CHD4
659 function at varying steps of SGN pathfinding. The candidate CHD4 binding sites include promoters and
660 enhancers that regulate the transcription of Eph receptors and Ephrin ligands. CHD4 and the NuRD
661 subunits HDAC1/2 may impose a repressive epigenetic state on these cis-regulatory elements to
662 attenuate transcription. Inactivation of CHD4 increases transcript levels of axon guidance genes to
663 perturb the stereotypic peripheral axon patterning. These results also have a broader implication on other
664 neuronal circuits in patients with SIHIWES, where subtle changes may be more challenging to define.

665 **Conflict of Interest:**

666 The authors declared no potential conflicts of interest to the research, authorship, and publication of this
667 article.

668

669 **Accession Numbers:**

670 The GEO accession number for the CUT&Tag raw fastq data, along with the processed bigwig and
671 SEACR peak files, is GSE250033. IGV session with the CUT&Tag tracks can be provided upon request.

672

673 **Author contribution:**

674 JK and EM designed, performed experiments, acquired and analyzed immunofluorescent images. JN
675 performed CUT&Tag and JQ analyzed data from CUT&Tag. KYK assisted in data analysis on CUT&Tag
676 and RNAscope. KYK conceived the project and assisted with the analysis. JK, EM, and KYK wrote the
677 manuscript.

678

679 **Acknowledgments:**

680 We thank Dr. Katia Georgopoulos (Mass General Hospital) and Dr. Lisa Goodrich (Harvard Medical
681 School) for providing the *Chd4*$^{flox/flox}$ animals and advice on dosing the Ngn1 CreER^{T2} animals,
682 respectively. We acknowledge Dr. Alejandra Laureano and Ms. Anna Maria Hinman for initially
683 generating and maintaining the mouse line. NIH R01 DC015000 supported this work to KYK.

Fig. 1

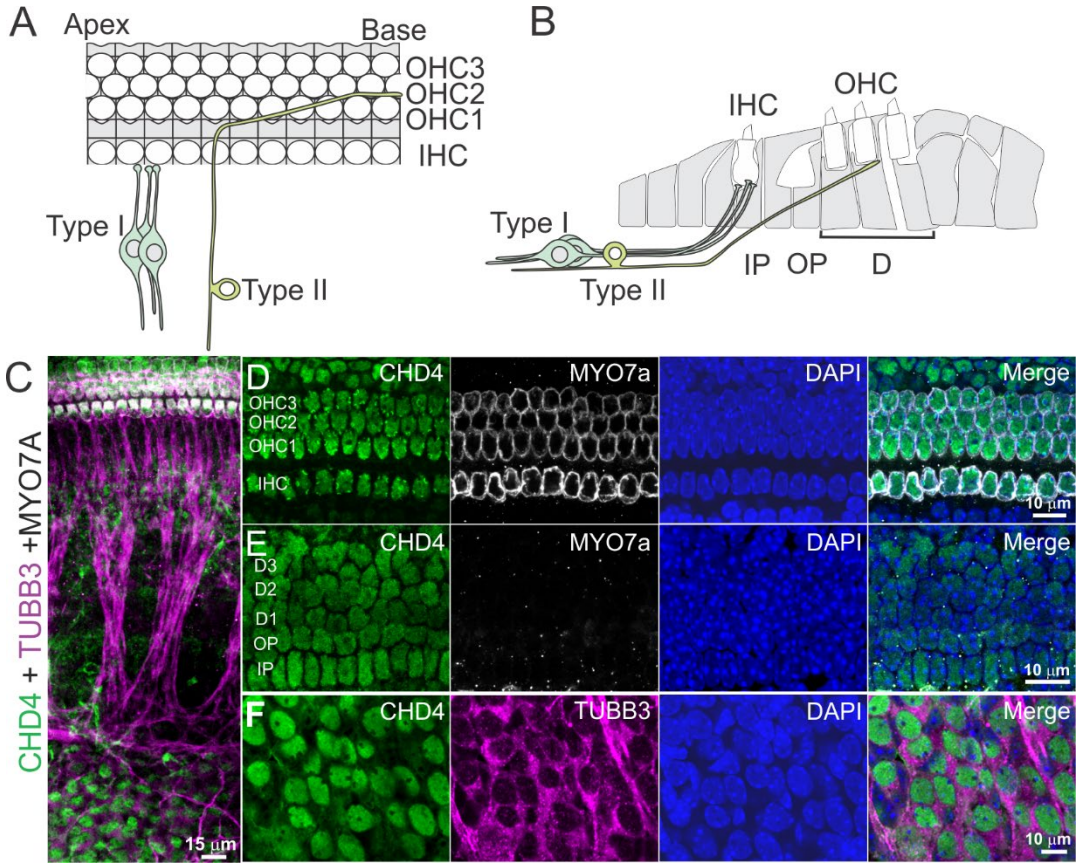
A
Apex
Base
OHC3
OHC2
OHC1
IHC
Type I
Type II
B
IHC
OHC
Type I
Type II
IP
OP
D
C
CHD4 + TUBB3 +MYO7A
15 µm
D
CHD4
MYO7a
DAPI
Merge
OHC3
OHC2
OHC1
IHC
10 µm
E
CHD4
MYO7a
DAPI
Merge
D3
D2
D1
OP
IP
10 µm
F
CHD4
TUBB3
DAPI
Merge
10 µm

Fig. 2

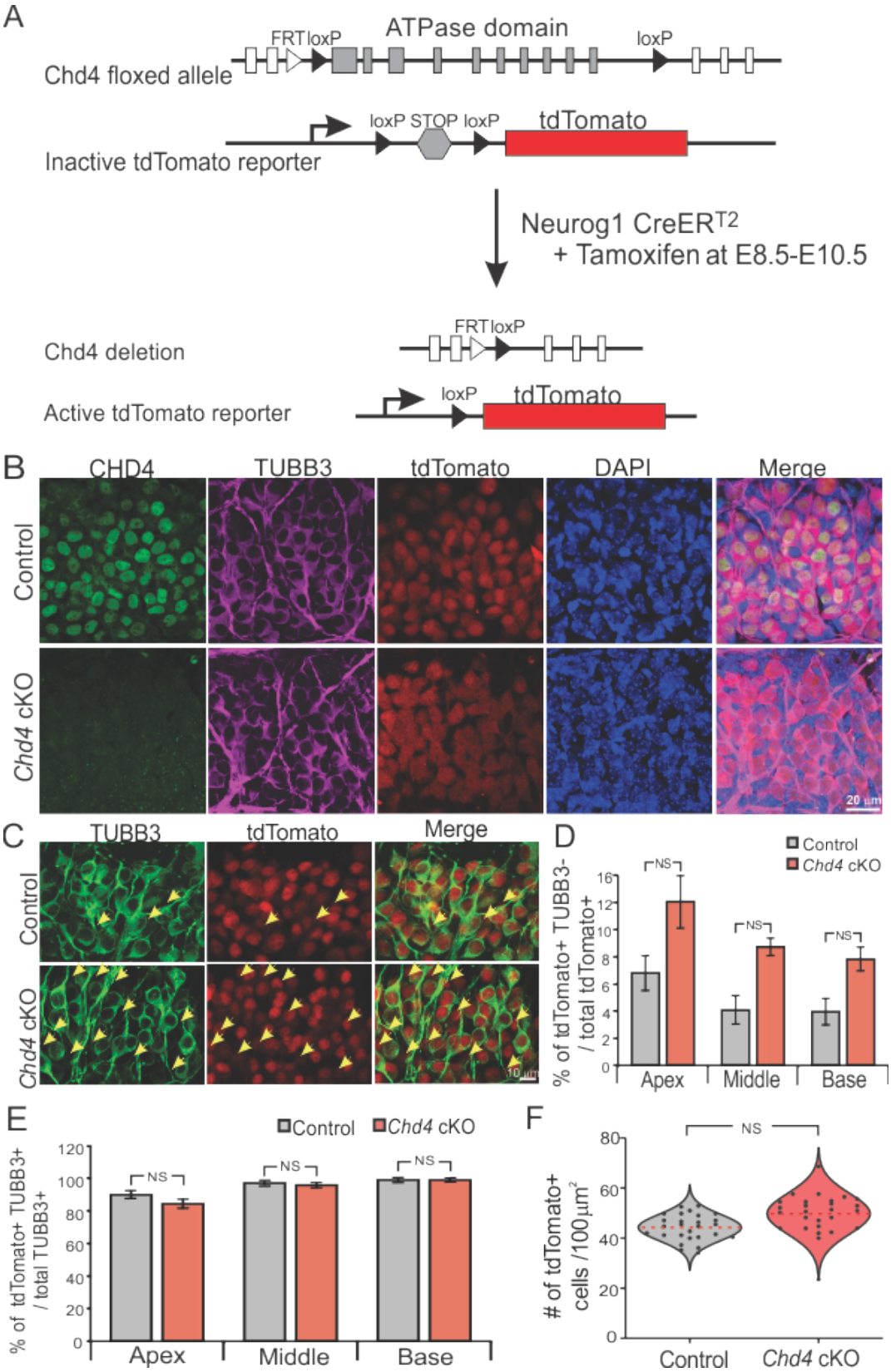
A
Chd4 floxed allele
FRT loxP
ATPase domain
loxP
Inactive tdTomato reporter
loxP STOP loxP
tdTomato
Neurog1 CreERT2
+ Tamoxifen at E8.5-E10.5
Chd4 deletion
FRT loxP
Active tdTomato reporter
loxP
tdTomato
B
CHD4
TUBB3
tdTomato
DAPI
Merge
Control
Chd4 cKO
20 µm
C
TUBB3
tdTomato
Merge
Control
Chd4 cKO
10 µm
D
Control
Chd4 cKO
% of tdTomato+ TUBB3- / total tdTomato+
NS
Apex
Middle
Base
E
Control
Chd4 cKO
% of tdTomato+ TUBB3+ / total TUBB3+
NS
Apex
Middle
Base
F
NS
# of tdTomato+ cells /100µm²
Control
Chd4 cKO

Figure 3

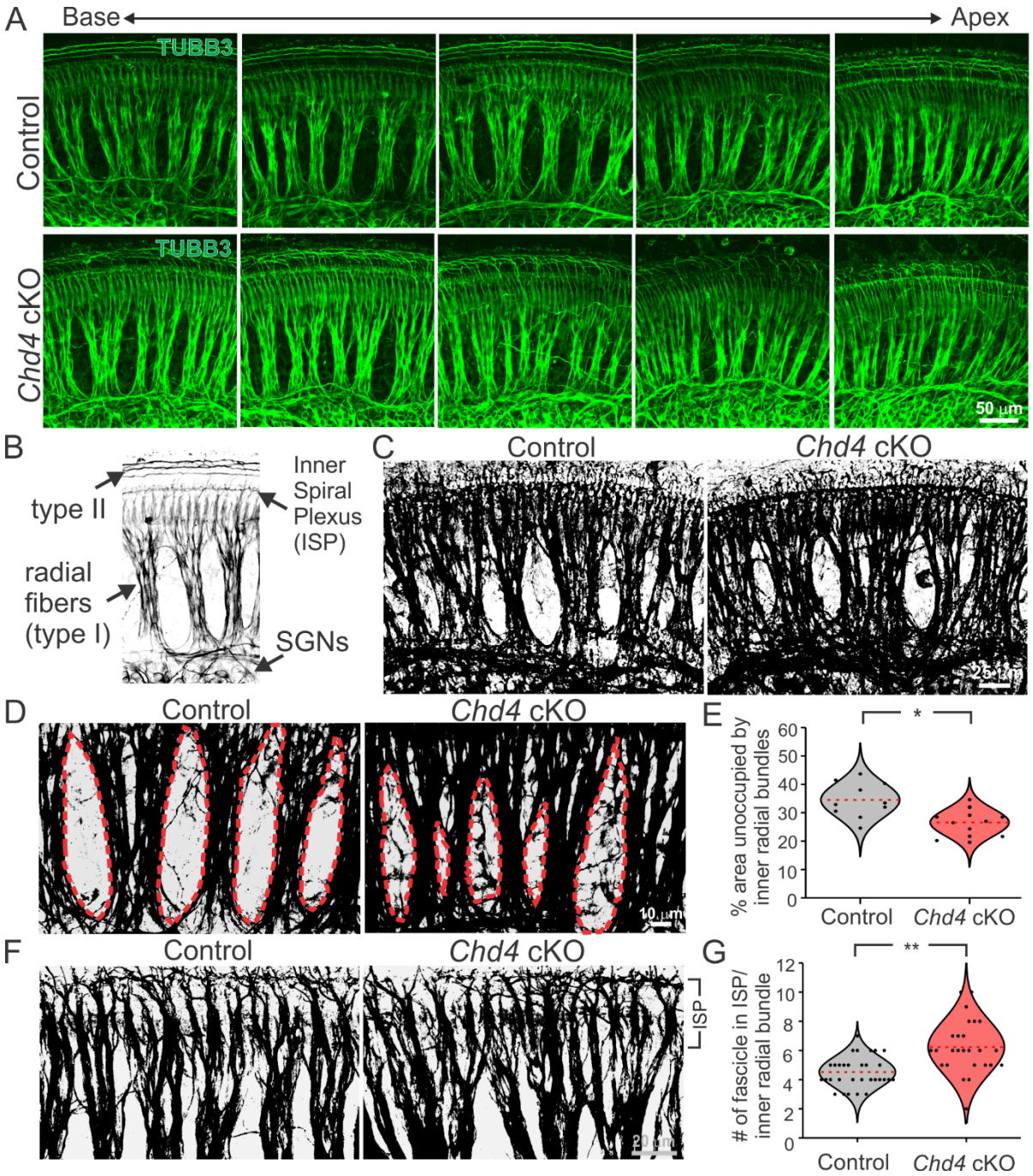
A
Base
Apex
TUBB3
Control
TUBB3
Chd4 cKO
50 µm
B
type II
Inner Spiral Plexus (ISP)
radial fibers (type I)
SGNs
C
Control
Chd4 cKO
25 µm
D
Control
Chd4 cKO
10 µm
E
*
% area unoccupied by inner radial bundles
60
50
40
30
20
10
0
Control
Chd4 cKO
F
Control
Chd4 cKO
ISP
G
**
# of fascicle in ISP/ inner radial bundle
12
10
8
6
4
2
0
Control
Chd4 cKO

Figure 4.

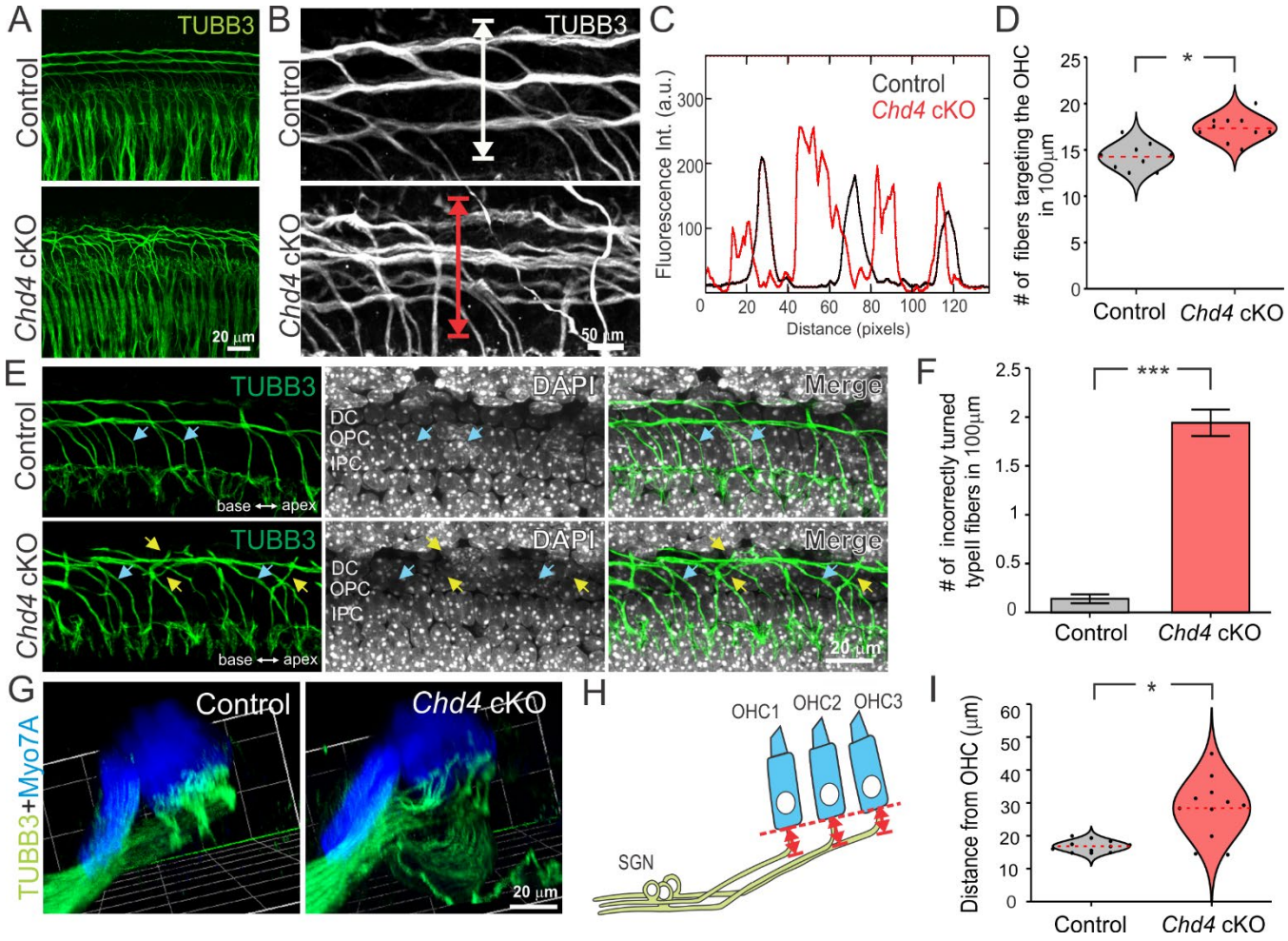
A
TUBB3
Control
Chd4 cKO
20 µm
B
TUBB3
Control
Chd4 cKO
50 µm
C
Control
Chd4 cKO
Fluorescence Int. (a.u.)
Distance (pixels)
D
# of fibers targeting the OHC in 100µm
Control
Chd4 cKO
E
TUBB3
DAPI
Merge
DC
OPC
IPC
base ↔ apex
20 µm
F
# of incorrectly turned typell fibers in 100µm
Control
Chd4 cKO
G
Control
Chd4 cKO
TUBB3+Myo7A
20 µm
H
OHC1
OHC2
OHC3
SGN
I
Distance from OHC (µm)
Control
Chd4 cKO

Figure 5

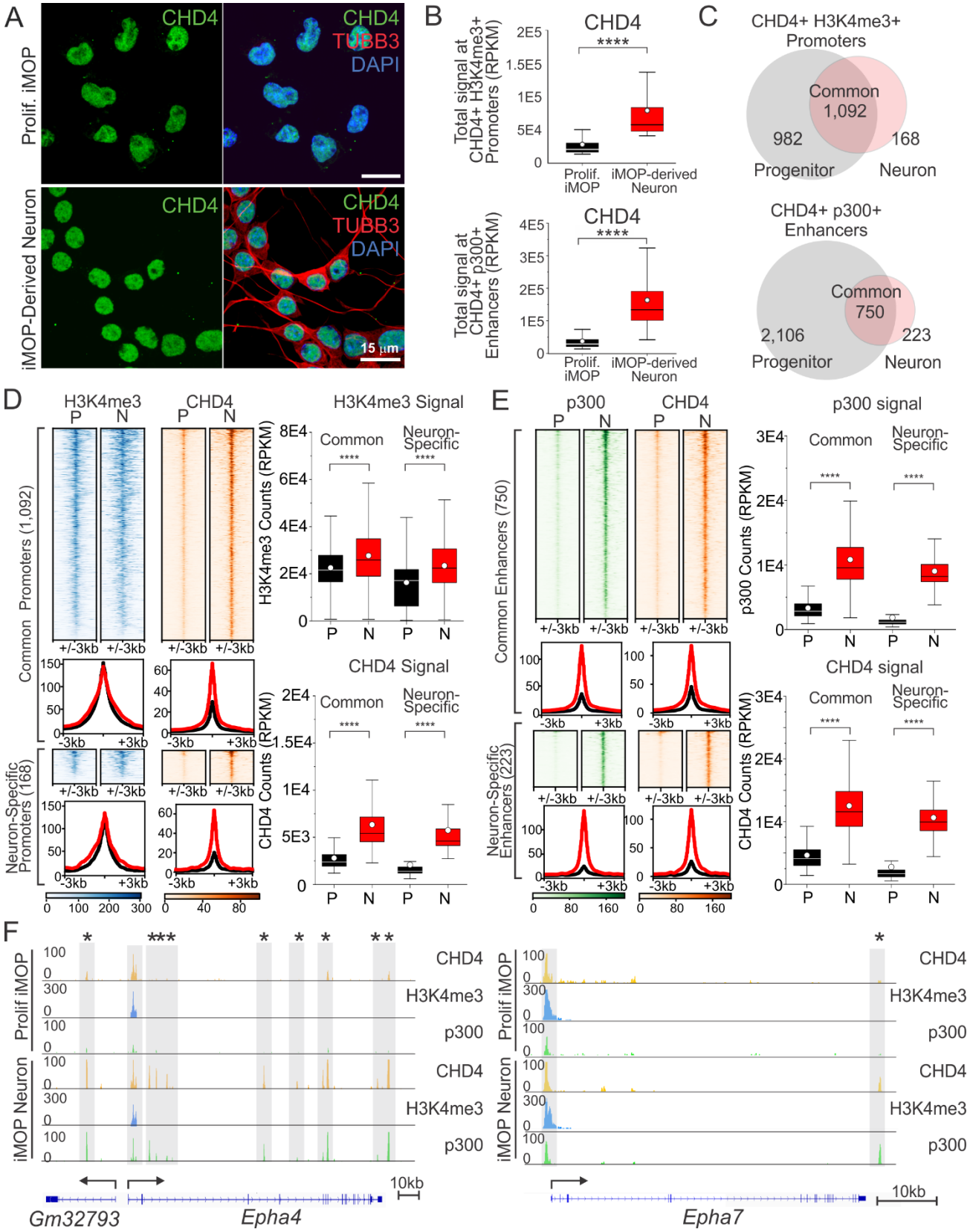
A
Prolif. iMOP
iMOP-Derived Neuron
CHD4
CHD4
TUBB3
DAPI
15 µm
B
CHD4
Total signal at CHD4+ H3K4me3+ Promoters (RPKM)
Total signal at CHD4+ p300+ Enhancers (RPKM)
Prolif. iMOP
iMOP-derived Neuron
C
CHD4+ H3K4me3+ Promoters
Common 1,092
982 Progenitor
168 Neuron
CHD4+ p300+ Enhancers
Common 750
2,106 Progenitor
223 Neuron
D
H3K4me3
CHD4
H3K4me3 Signal
CHD4 Signal
Common Promoters (1,092)
Neuron-Specific Promoters (168)
H3K4me3 Counts (RPKM)
CHD4 Counts (RPKM)
Common
Neuron-Specific
+/-3kb
-3kb
+3kb
E
p300
CHD4
p300 signal
CHD4 signal
Common Enhancers (750)
Neuron-Specific Enhancers (223)
p300 Counts (RPKM)
F
Prolif iMOP
iMOP Neuron
CHD4
H3K4me3
p300
10kb
Gm32793
Epha4
Epha7

Figure 6.

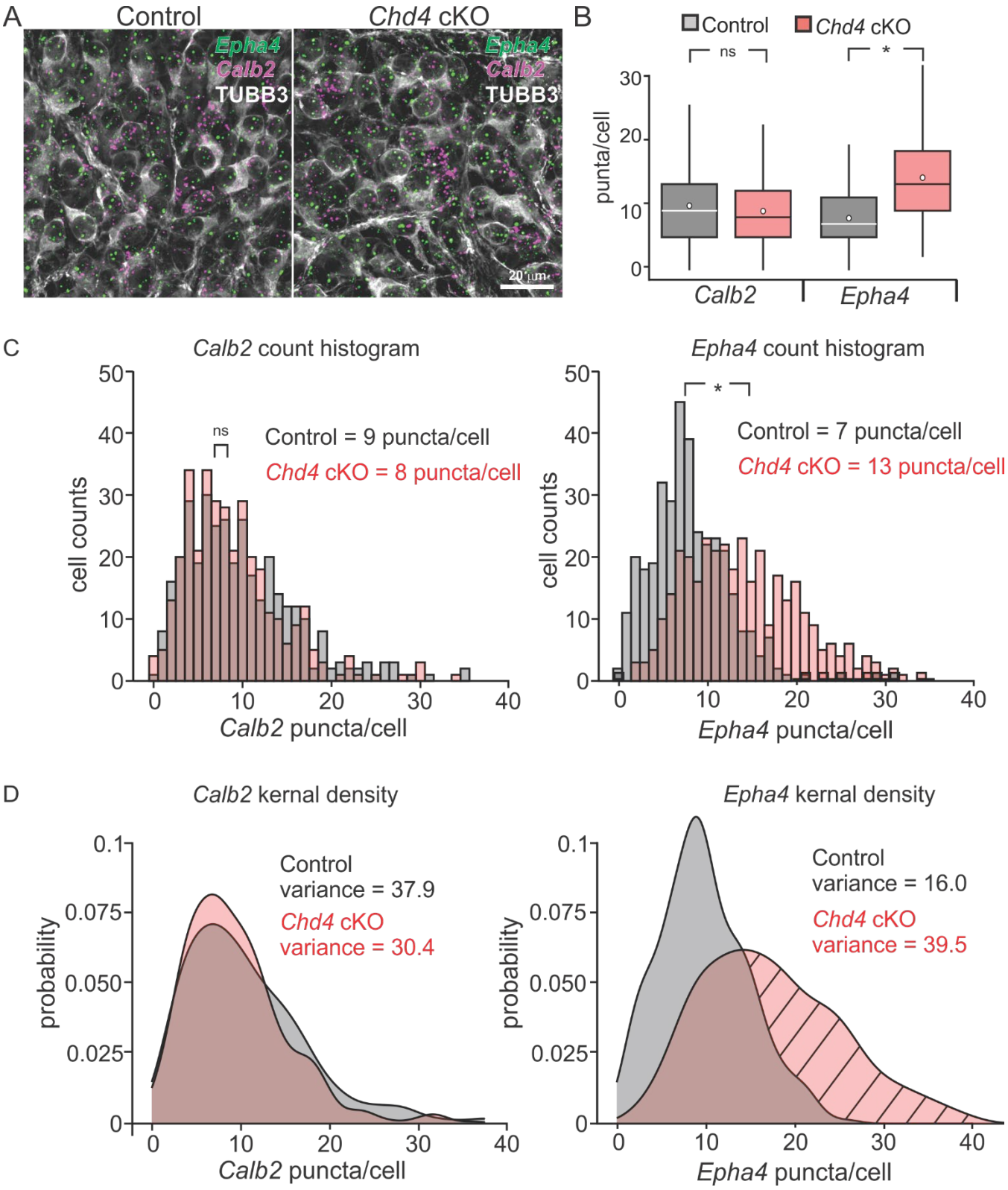
A
Control
Chd4 cKO
Epha4
Calb2
TUBB3
20 µm
B
Control
Chd4 cKO
ns
*
punta/cell
Calb2
Epha4
C
Calb2 count histogram
Control = 9 puncta/cell
Chd4 cKO = 8 puncta/cell
cell counts
Calb2 puncta/cell
Epha4 count histogram
Control = 7 puncta/cell
Chd4 cKO = 13 puncta/cell
Epha4 puncta/cell
D
Calb2 kernal density
Control
variance = 37.9
Chd4 cKO
variance = 30.4
probability
Epha4 kernal density
Control
variance = 16.0
Chd4 cKO
variance = 39.5

684 **Figure 1. CHD4 expression in the spiral ganglion and the organ of Corti.**

685 (A) Top-down schematic depicting the innervation pattern of type I and II SGNs. Type I SGNs extend
686 single, unbranched neurites that innervate an individual inner hair cell (IHC). Type II SGNs extend
687 neurites into the outer hair cell (OHC) region, turn basally, and can contact multiple OHCs. (B) Sagittal
688 schematic of the innervation pattern. Multiple Type I SGNs innervate a single IHC. Type II neurites make
689 a basal turn in the region near Deiters' cells, a supporting cell type. (C) Immunofluorescence labeling of
690 CHD4 (green), TUBB3 (magenta), and MYO7A (white) from a flat-mounted cochlea. TUBB3 and MYO7A
691 label neurons and hair cells, while DAPI (blue) marks nuclei. Different regions of immunolabeled E18.5
692 cochlea. (D) Expression of CHD4 in the single row of inner hair cells (IHC) and the three rows of outer
693 hair cells (OHC1-3). (E) CHD4 labeling in supporting cells, including inner pillar (IP), outer pillar (OP),
694 and three rows of Dieter cells (DC1-3). The nuclei of supporting cells reside underneath hair cells. (F)
695 CHD4 labeling in spiral ganglion neurons. Scale bar as marked.

696

697 **Figure 2. Deletion of *Chd4* from SGNs using Neurog1 CreER^{T2} Chd4 $^{flox/flox}$ mice.**

698 (A) Schematic illustration of Cre-mediated *Chd4* deletion following tamoxifen induction in *Chd4*
699 conditional knockout (cKO) mice containing Neurog1 CreER^{T2}; *Chd4*$^{flox/flox}$; tdTomato alleles.
700 Administration of tamoxifen at E8.5-E10.5 deletes loxP flanked exons coding for the *Chd4* ATPase
701 domain and activates expression of the tdTomato reporter. Animals without the *Chd4* cKO allele
702 (Neurog1 CreER^{T2}; tdTomato) were used as controls (B) Immunostaining of CHD4 and TUBB3 marked
703 neurons in E18.5 cochlea. tdTomato expression correlates with the presence of Cre activity. Nuclear
704 CHD4 expression was observed in DAPI-marked nuclei in control SGNs but was absent in *Chd4* cKO
705 SGNs after tamoxifen administration. (C) Confocal micrographs from the spiral ganglion. Yellow arrows
706 indicate tdTomato^{+} and TUBB3^{-} cells. (D) Percentages of tdTomato^{+} and TUBB3^{-} cells found within the
707 apex, middle, and base regions of the cochlea (apex, $p<0.136$, middle, $p<0.095$; base, $p<0.148$; control,
708 n=3 and Chd4 cKO, n=3 cochlea) (E) Percentages of cells expressing tdTomato and TUBB3 from the
709 base to apex of the cochlea from control and *Chd4* cKO cochleae (apex $p<0.302$; middle $p<0.603$; base,

710 p<0.9; control, n=3 and Chd4 cKO, n=3 cochleae) (F) Normalized number of tdTomato$^+$ cells per 100
711 μm^2 area in control and Chd4 cKO cochleae (p<0.081; control, n=27 and *Chd4* cKO n=27 images were
712 analyzed from control, n=3 and *Chd4* cKO, n=3 cochleae).The Student's t-test test was used for statistical
713 analysis using the number of cochleae. Scale bar as marked.
714
715 **Figure 3. Inner radial bundles display fasciculation defects in *Chd4* cKO cochleae**
716 (A) TUBB3 labeled cochleae from E18.5 control and *Chd4* cKO animals. Images are ordered from base
717 to apex. (B) Depiction of the inner spiral plexus (ISP) near the base of inner hair cells and peripheral
718 projections from type I (radial fibers) and II SGNs from E18.5 cochlea. (C) Binarized images of TUBB3
719 labeled control and *Chd4* cKO cochleae at E18.5. (D) Regions between radial fiber bundles were outlined
720 in red. (E) The identified areas were quantified and compared between control and *Chd4* cKO (p<0.049;
721 control, n=10 and *Chd4* cKO n=13 images were analyzed from control, n=3 and *Chd4* cKO, n=3
722 cochleae). (F) Binarized images of control and *Chd4* cKO E18.5 cochleae around the ISP. (G)
723 Comparison of the normalized number of fascicles in the ISP per radial bundle between control and *Chd4*
724 cKO cochleae (p<0.008; control, n=31 and *Chd4* cKO n=26 bundles were analyzed from control, n=5 and
725 *Chd4* cKO, n=3 cochleae). The Student's t-test was used for statistical analysis. Scale bars as marked.
726
727 **Figure 4. Type II spiral ganglion neurons display turning defects in the *Chd4* cKO mice.**
728 (A) TUBB3 labeled neuronal projections in E18.5 control and *Chd4* cKO cochleae**.** Type II fibers can be
729 distinguished by their anatomical location. (B) Type II fibers from control show stereotypic tracks that turn
730 towards the base and travel along individual rows of outer hair cells. *Chd4* cKO type II fibers showed
731 aberrant fiber tracks. (C) The intensity profile plot was measured along the white and red lines to highlight
732 the differences between the control and Chd4 cKO fiber tracks. Peaks from fluorescence intensity
733 measurements indicate the presence of a fiber track. Control cochleae show three peaks correlating with
734 fibers along the three rows of outer hair cells. Chd4 cKO samples showed an additional peak suggesting
735 aberrant fiber tracks (D) Normalized number of fibers entering the OHC region per 100 μm from control

736 and *Chd4* cKO E18.5 cochleae ($p<0.027$; control, n=9 and *Chd4* cKO n=10 images were analyzed from
737 control, n=3 and *Chd4* cKO, n=3 cochleae). (E) Optical section from TUBB3 and DAPI labeled confocal
738 micrographs that visualize fibers entering the OHC region. Blue arrows mark correctly turned while yellow
739 arrows show incorrect turning type II fibers. (F) The normalized number of incorrectly turned type II fibers
740 per 100 μm from control and *Chd4* cKO E18.5 cochleae ($p=2.82 \times 10^{-4}$; control, n=3 and *Chd4* cKO, n=3
741 cochleae). (G) 3D-rendered images highlighting the axonal trajectory from SGNs ($TUBB3^+$, green) to hair
742 cells ($MYO7A^+$, blue). (H) Schematic of peripheral SGN axonal projections to outer hair cells. Red arrows
743 represent the distance between contact points in the OHCs (red dashed line) and the final turning point
744 on the incoming axon. (I) Average distances from the base of outer hair cells to the axon bundles showed
745 differences between control and *Chd4* cKO ($p<0.034$; control, n=11, and *Chd4* cKO n=11 images were
746 analyzed from control, n=3 and *Chd4* cKO, n=3 cochleae). The Student's t-test was used for statistical
747 analysis. Scale bars as marked.
748
749 **Figure 5. CHD4 binds to the promoters of genes involved in axon guidance, including members**
750 **of the ephrin family of signaling molecules, in iMOP-derived neurons.**
751 (A) Overlap of CHD4 in the nuclei (DAPI) of proliferating iMOP and TUBB3 labeled iMOP-derived
752 neurons. CUT&Tag was performed using proliferating iMOP cells and iMOP-derived neurons. CUT&Tag
753 peaks were identified using SEACR. (B) Box and whisker plots show SEACR total signals for CHD4 at
754 CHD4+ H3K4me3+ and CHD4+p300+ in proliferating iMOPs were significantly different from that in
755 iMOP-derived neurons, $p<2.2 \times 10^{-16}$. (C) Venn diagrams show the overlap of CHD4+ H3K4me3+
756 promoters and CHD4+ p300+ enhancers between progenitors (P) and neurons (N). (D) Heatmaps and
757 profile plots show H3K4me3 and CHD4 signals within +/- 3kb of the summit regions of common and
758 neuron-specific promoters. Box and whisker plots show significantly increased H3K4me3 and CHD4
759 signals at both common and neuron-specific promoters in P compared to N. (E) Heatmaps and profile
760 plots show p300 and CHD4 signals within +/- 3kb of the summit regions of common and neuron-specific
761 enhancers. Box and whisker plots showing significantly increased p300 and CHD4 signals at both

762 common and neuron-specific enhancers in P compared to that in N. (F) Enrichment of CHD4 (orange),
763 H3K4me3 (blue), and p300 (green) at the specified genomic region of *Epha4* and *Epha7* in proliferating
764 iMOPs and iMOP-derived neurons. Highlighted genomic regions represent H3K4me3 marked promoters.
765 Highlighted regions with asterisks denote the regions with increased enrichment of CHD4 and p300 in
766 iMOP-derived neurons. The number of asterisks denotes the peaks with increased CHD4 and p300
767 levels. Wilcoxon rank-sum test was used for statistical analysis. Scale bars as marked.
768
769 **Figure 6. *Chd4* cKO shows increased *Epha4* mRNA expression in SGNs.**
770 (A) E16.5 control and mutant cochlea processed for RNA fluorescence *in situ* hybridization (FISH) with
771 probes against *Epha4* and *Calb2.* Cochleae were immunolabeled with TUBB3 to visualize SGNs. (B) The
772 number of puncta for individual TUBB3 labeled cells was quantified. The lines denoted median values,
773 and the circles represented mean values. Controls were compared to *Chd4* cKO samples after
774 performing smFISH for *Calb2* ($p<0.295$) and Epha4 ($p<0.011$; control, n=3 and *Chd4* cKO, n=3 cochlea).
775 *Calb2* was used as a transcript to mark the SGNs, while *Epha4* was used as a CHD4 target gene.
776 Distribution of the number of smFISH puncta in control and *Chd4* cKO SGNs for (C) *Calb2* and *Epha4*
777 transcripts in SGNs (control, n=350 and *Chd4* cKO n=345 cells were counted from control, n=3 and *Chd4*
778 cKO, n=3 cochleae). (D) Kernal densities for *Calb2* and *Epha4* transcripts. Significant non-overlapping
779 regions of densities in Epha4 (hashed region) display an increased probability of cells from Chd4 cKO
780 with higher levels of Epha4 transcripts compared to the control. Wilcoxon rank-sum test was used for
781 statistical analysis. Scale bars as marked.
782

Fig. S1

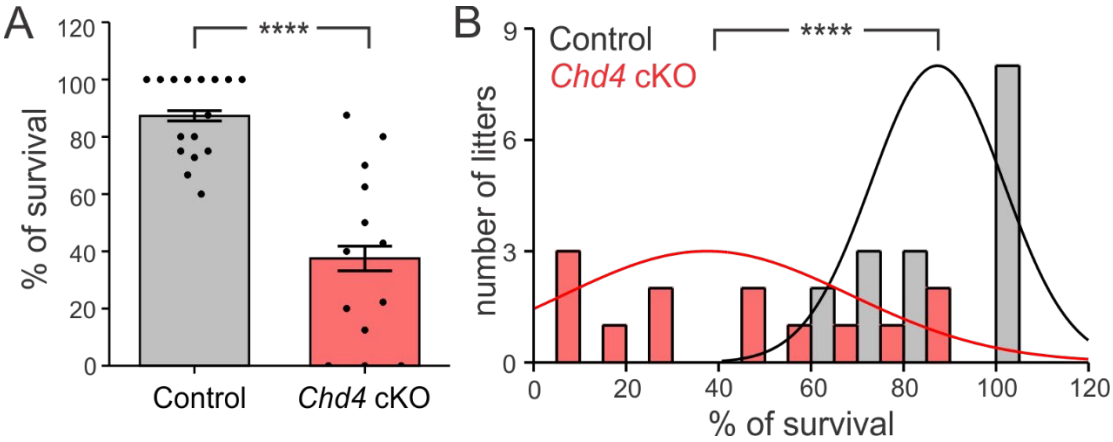
A
120
100
80
60
40
20
0
% of survival
****
Control
Chd4 cKO
B
9
6
3
0
number of litters
Control
Chd4 cKO
****
0
20
40
60
80
100
120
% of survival

Fig. S2

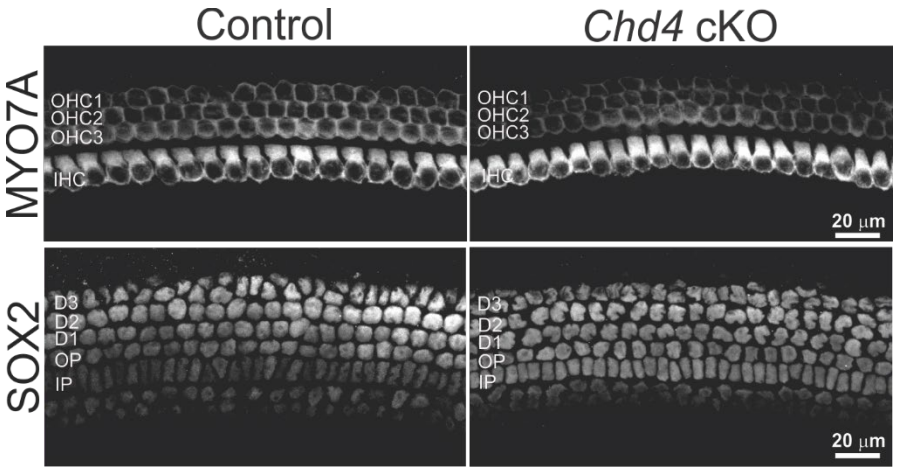
Control
Chd4 cKO
MYO7A
OHC1
OHC2
OHC3
IHC
OHC1
OHC2
OHC3
IHC
20 μm
SOX2
D3
D2
D1
OP
IP
D3
D2
D1
OP
IP
20 μm

Fig. S3

A

ID	Description	p value
0048013	ephrin receptor signaling pathway	4.9E-05
0007411	axon guidance	2.0E-13
1902287	semaphorin-plexin signaling pathway involved in axon guidance	2.7E-02
0007409	axonogenesis	1.6E-14
0006325	chromatin organization	5.1E-14
0007413	axonal fasciculation	1.6E-02

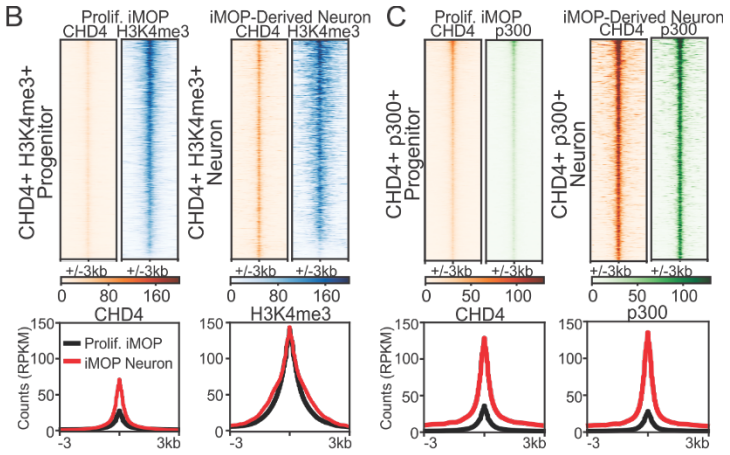

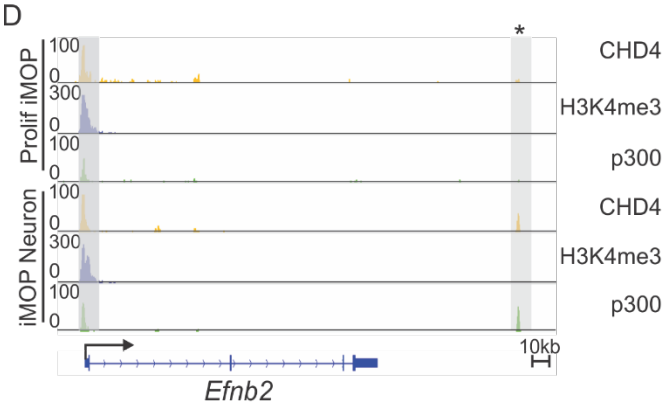

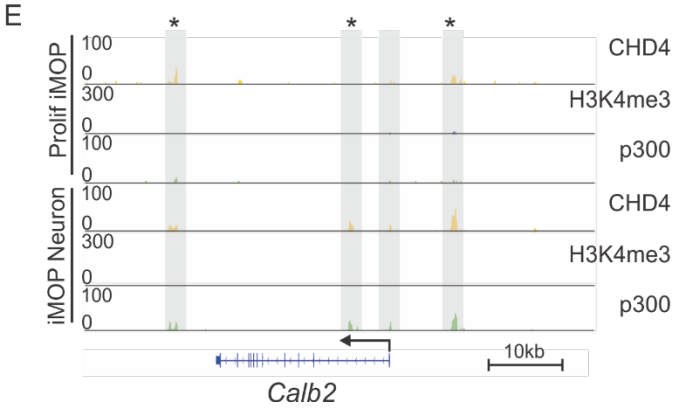

783 **Supplemental Figure Legend**

784

785 **Supplemental Figure 1. Survival of *Chd4* conditional knockout mice.**

786 (A) Average percentage of viable pups from all collected control and mutant litters ($p<4.36 \times 10^{-6}$; control,
787 n=16 and *Chd4* cKO, n=13 litters). (B) Distribution of the percentages of surviving E18.5 pups from control
788 and *Chd4* cKO litters after tamoxifen treatment. The p-value and sample size as listed. The Student's t-
789 test was used for statistical analysis.

790

791 **Supplemental Figure 2. The number of supporting and hair cells is unaffected following the**
792 **deletion of *Chd4* within spiral ganglion neurons.**

793 Immunofluorescent labeling of MYO7A and SOX2 marked hair cells and supporting cells from E18.5
794 cochleae. Confocal stacks from control and *Chd4* cKO cochleae with MYO7A marked hair cells and
795 SOX2 marked supporting cells. OHC = outer hair cell, IHC = inner hair cell, D = Deiters' cells, OP = outer
796 phalangeal cells, IP = inner phalangeal cells. Scale bar as marked.

797

798 **Supplemental Figure 3. Identifying CHD4 binding at promoters and enhancers of target genes.**

799 (A) Table showing Gene Ontology ID, description of each category, and corresponding adjusted p values
800 using Benjamini-Hochberg method for multiple testing correction. (B) Heatmaps and profile plots of CHD4
801 and H3K4me3 signals within +/- 3kb of the summit regions of CHD4+ H3K4me3+ in both proliferating
802 iMOP and iMOP-derived neurons. (C) Heatmaps and profile plots of CHD4 and p300 signals within +/-
803 3kb of the summit regions of CHD4+ p300+ in prolif. iMOP and iMOP-derived neurons. (D Enrichment of
804 CHD4 (orange), H3K4me3 (blue), and p300 (green) at the specified genomic regions of *Efnb2* in
805 proliferating iMOPs and iMOP-derived neurons. Highlighted genomic regions represented H3K4me3
806 marked promoters, while highlighted regions with asterisks denote regions with increased CHD4 and
807 p300 in iMOP-derived neurons. The number of asterisks indicate the number of peaks that show
808 increased CHD4 and p300 levels. Scale bars as marked.

Table 1

Allele	Sequence (5'->3')	Amplicon Size
Chd4	TCC AGA AGA AGA CGG CAG AT	Wild-type: 275bp Chd4 floxed allele: 400bp
	CTG GTC ATA GGG CAG GTC TC	
Ai9 tdTomato	AAG GGA GCT GCA GTG GAG TA	Wild-type: 287bp
	CCG AAA ATC TGT GGG AAG TC	
	GGC ATT AAA GCA GCG TAT CC	Mutant: 196bp
	CTG TTC CTG TAC GGC ATG G	
Generic Cre	AGC GAT CGC TGC CAG GAT	Mutant: 382bp
	ACC AGC GTT TTC GTT CTG CC	
Neurogenin1-specific Cre	AGC CCA TTC ACT CCC TGA G	Mutant: 527bp
	ATC AAC GTT TTC TTT TCG GA	

Table 2

Antibody	Company	Identifier	Dilution	Purpose
mouse anti-CHD4	Abcam	Cat# ab70469, RRID:AB_2229454	1:100 (tissue) 1:300 (cells)	Immunostaining
rabbit anti-MYO7A	Proteus Bioscience	Cat# 25-6790, RRID:AB_10015251	1:200	Immunostaining
mouse anti-Tuj1 (TUBB3)	BioLegend	Cat# 801202, RRID:AB_10063408	1:300	Immunostaining
rabbit anti-Tuj1 (TUBB3)	BioLegend	Cat# 802001, RRID:AB_2564645	1:300	Immunostaining
rabbit anti-Sox2	Millipore	Cat# AB5603, RRID:AB_2286686	1:100	Immunostaining
goat anti-mouse Alexa 488	Thermo Fisher Scientific	Cat# A-11001, RRID:AB_2534069	1:500	Immunostaining
goat anti-mouse Alexa 647	Thermo Fisher Scientific	Cat# A-21235, RRID:AB_2535804	1:500	Immunostaining
goat anti-rabbit Alexa 488	Thermo Fisher Scientific	Cat# A-11034, RRID:AB_2576217	1:500	Immunostaining
goat anti-rabbit Alexa 647	Thermo Fisher Scientific	Cat# A-21246, RRID:AB_2535814	1:500	Immunostaining
goat anti-rabbit Alexa 568	Thermo Fisher Scientific	Cat# A-11011, RRID:AB_143157	1:500	Immunostaining
Rabbit anti-EP300 (p300)	Developmental Studies Hybridoma Bank (DSHB)	Cat# ENCITp300-1, RRID:AB_2619604	1:50	CUT&Tag
rabbit anti-H3K4me3	Active Motif	Cat# 39060, RRID: AB_2615077	1:50	CUT&Tag
Rabbit anti-CHD4	Abcam	Cat# ab72418, RRID:AB_1268107	1:50	CUT&Tag
rabbit IgG	Jackson ImmunoResearch	Cat# 011-000-003, RRID:AB_2337118	1:50	CUT&Tag

Table 3

RNAscope Probe	Accession Number	Probe Region	Catalog Number
Mm-Calb2	NM_007586.1	147-1265	313641
Mm-Epha4	NM_007936.3	291-1191	419081

809 **References**

810 **Adamson, C. L., Reid, M. A., Mo, Z. L., Bowne-English, J. and Davis, R. L.** (2002). Firing features and
811 potassium channel content of murine spiral ganglion neurons vary with cochlear location. *J*
812 *Comp Neurol* **447**, 331-350.
813 **Appler, J. M. and Goodrich, L. V.** (2011). Connecting the ear to the brain: Molecular mechanisms of
814 auditory circuit assembly. *Prog Neurobiol* **93**, 488-508.
815 **Borg, E., Engstrom, B., Linde, G. and Marklund, K.** (1988). Eighth nerve fiber firing features in normal-
816 hearing rabbits. *Hear Res* **36**, 191-201.
817 **Bornelov, S., Reynolds, N., Xenophontos, M., Gharbi, S., Johnstone, E., Floyd, R., Ralser, M., Signolet,**
818 **J., Loos, R., Dietmann, S., et al.** (2018). The Nucleosome Remodeling and Deacetylation
819 Complex Modulates Chromatin Structure at Sites of Active Transcription to Fine-Tune Gene
820 Expression. *Mol Cell* **71**, 56-72 e54.
821 **Bruce, L. L., Kingsley, J., Nichols, D. H. and Fritzsch, B.** (1997). The development of vestibulocochlear
822 efferents and cochlear afferents in mice. *Int J Dev Neurosci* **15**, 671-692.
823 **Chen, W. C., Xue, H. Z., Hsu, Y. L., Liu, Q., Patel, S. and Davis, R. L.** (2011). Complex distribution
824 patterns of voltage-gated calcium channel alpha-subunits in the spiral ganglion. *Hear Res* **278**,
825 52-68.
826 **Clapier, C. R., Iwasa, J., Cairns, B. R. and Peterson, C. L.** (2017). Mechanisms of action and regulation
827 of ATP-dependent chromatin-remodelling complexes. *Nat Rev Mol Cell Biol* **18**, 407-422.
828 **Coate, T. M., Raft, S., Zhao, X., Ryan, A. K., Crenshaw, E. B., 3rd and Kelley, M. W.** (2012). Otic
829 mesenchyme cells regulate spiral ganglion axon fasciculation through a Pou3f4/EphA4 signaling
830 pathway. *Neuron* **73**, 49-63.
831 **Coate, T. M., Spita, N. A., Zhang, K. D., Isgrig, K. T. and Kelley, M. W.** (2015). Neuropilin-
832 2/Semaphorin-3F-mediated repulsion promotes inner hair cell innervation by spiral ganglion
833 neurons. *Elife* **4**.
834 **Deans, M. R.** (2022). Planar cell polarity signaling guides cochlear innervation. *Dev Biol* **486**, 1-4.
835 **Defourny, J., Poirrier, A. L., Lallemend, F., Mateo Sanchez, S., Neef, J., Vanderhaeghen, P., Soriano, E.,**
836 **Peuckert, C., Kullander, K., Fritzsch, B., et al.** (2013). Ephrin-A5/EphA4 signalling controls
837 specific afferent targeting to cochlear hair cells. *Nat Commun* **4**, 1438.
838 **el Barbary, A.** (1991). Auditory nerve of the normal and jaundiced rat. I. Spontaneous discharge rate
839 and cochlear nerve histology. *Hear Res* **54**, 75-90.
840 **Ghimire, S. R. and Deans, M. R.** (2019). Frizzled3 and Frizzled6 Cooperate with Vangl2 to Direct
841 Cochlear Innervation by Type II Spiral Ganglion Neurons. *J Neurosci* **39**, 8013-8023.
842 **Ghimire, S. R., Ratzan, E. M. and Deans, M. R.** (2018). A non-autonomous function of the core PCP
843 protein VANGL2 directs peripheral axon turning in the developing cochlea. *Development* **145**.
844 **Hoffmeister, H., Fuchs, A., Erdel, F., Pinz, S., Grobner-Ferreira, R., Bruckmann, A., Deutzmann, R.,**
845 **Schwartz, U., Maldonado, R., Huber, C., et al.** (2017). CHD3 and CHD4 form distinct NuRD
846 complexes with different yet overlapping functionality. *Nucleic Acids Res* **45**, 10534-10554.
847 **Hosokawa, H., Tanaka, T., Suzuki, Y., Iwamura, C., Ohkubo, S., Endoh, K., Kato, M., Endo, Y.,**
848 **Onodera, A., Tumes, D. J., et al.** (2013). Functionally distinct Gata3/Chd4 complexes
849 coordinately establish T helper 2 (Th2) cell identity. *Proc Natl Acad Sci U S A* **110**, 4691-4696.
850 **Huang, D., Sherman, B. T. and Lempicki, R. A.** (2009). Systematic and integrative analysis of large gene
851 lists using DAVID bioinformatics resources. *Nat Protoc* **4**, 44-57.

852 **Huang, L. C., Barclay, M., Lee, K., Peter, S., Housley, G. D., Thorne, P. R. and Montgomery, J. M.**
853 (2012). Synaptic profiles during neurite extension, refinement and retraction in the developing
854 cochlea. *Neural Dev* **7**, 38.
855 **Hung, H., Kohnken, R. and Svaren, J.** (2012). The nucleosome remodeling and deacetylase chromatin
856 remodeling (NuRD) complex is required for peripheral nerve myelination. *J Neurosci* **32**, 1517-
857 1527.
858 **Kent, W. J., Zweig, A. S., Barber, G., Hinrichs, A. S. and Karolchik, D.** (2010). BigWig and BigBed:
859 enabling browsing of large distributed datasets. *Bioinformatics* **26**, 2204-2207.
860 **Kiang, N. Y., Pfeiffer, R. R., Warr, W. B. and Backus, A. S.** (1965). Stimulus Coding in the Cochlear
861 Nucleus. *Ann Otol Rhinol Laryngol* **74**, 463-485.
862 **Kim, E. J., Hori, K., Wyckoff, A., Dickel, L. K., Koundakjian, E. J., Goodrich, L. V. and Johnson, J. E.**
863 (2011). Spatiotemporal fate map of neurogenin1 (Neurog1) lineages in the mouse central
864 nervous system. *J Comp Neurol* **519**, 1355-1370.
865 **Kim, Y. J., Ibrahim, L. A., Wang, S. Z., Yuan, W., Evgrafov, O. V., Knowles, J. A., Wang, K., Tao, H. W.**
866 **and Zhang, L. I.** (2016). EphA7 regulates spiral ganglion innervation of cochlear hair cells. *Dev*
867 *Neurobiol* **76**, 452-469.
868 **Koundakjian, E. J., Appler, J. L. and Goodrich, L. V.** (2007). Auditory neurons make stereotyped wiring
869 decisions before maturation of their targets. *J Neurosci* **27**, 14078-14088.
870 **Kwan, K. Y., Shen, J. and Corey, D. P.** (2015). C-MYC transcriptionally amplifies SOX2 target genes to
871 regulate self-renewal in multipotent otic progenitor cells. *Stem Cell Reports* **4**, 47-60.
872 **Langmead, B. and Salzberg, S. L.** (2012). Fast gapped-read alignment with Bowtie 2. *Nat Methods* **9**,
873 357-359.
874 **Layman, W. S., Sauceda, M. A. and Zuo, J.** (2013). Epigenetic alterations by NuRD and PRC2 in the
875 neonatal mouse cochlea. *Hear Res* **304**, 167-178.
876 **Layman, W. S. and Zuo, J.** (2014). Epigenetic regulation in the inner ear and its potential roles in
877 development, protection, and regeneration. *Front Cell Neurosci* **8**, 446.
878 **Li, H., Handsaker, B., Wysoker, A., Fennell, T., Ruan, J., Homer, N., Marth, G., Abecasis, G., Durbin, R.**
879 **and Genome Project Data Processing, S.** (2009). The Sequence Alignment/Map format and
880 SAMtools. *Bioinformatics* **25**, 2078-2079.
881 **Liberman, M. C.** (1978). Auditory-nerve response from cats raised in a low-noise chamber. *J Acoust Soc*
882 *Am* **63**, 442-455.
883 **----** (1982). Single-neuron labeling in the cat auditory nerve. *Science* **216**, 1239-1241.
884 **Liu, Q., Manis, P. B. and Davis, R. L.** (2014). I h and HCN channels in murine spiral ganglion neurons:
885 tonotopic variation, local heterogeneity, and kinetic model. *J Assoc Res Otolaryngol* **15**, 585-
886 599.
887 **Liu, W. and Davis, R. L.** (2014). Calretinin and calbindin distribution patterns specify subpopulations of
888 type I and type II spiral ganglion neurons in postnatal murine cochlea. *J Comp Neurol* **522**, 2299-
889 2318.
890 **Low, J. K., Webb, S. R., Silva, A. P., Saathoff, H., Ryan, D. P., Torrado, M., Brofelth, M., Parker, B. L.,**
891 **Shepherd, N. E. and Mackay, J. P.** (2016). CHD4 Is a Peripheral Component of the Nucleosome
892 Remodeling and Deacetylase Complex. *J Biol Chem* **291**, 15853-15866.
893 **Lu, C. C., Appler, J. M., Houseman, E. A. and Goodrich, L. V.** (2011). Developmental profiling of spiral
894 ganglion neurons reveals insights into auditory circuit assembly. *J Neurosci* **31**, 10903-10918.

895 **Madisen, L., Zwingman, T. A., Sunkin, S. M., Oh, S. W., Zariwala, H. A., Gu, H., Ng, L. L., Palmiter, R.**
896 **D., Hawrylycz, M. J., Jones, A. R., et al.** (2010). A robust and high-throughput Cre reporting and
897 characterization system for the whole mouse brain. *Nat Neurosci* **13**, 133-140.
898 **Martinez-Monedero, R., Liu, C., Weisz, C., Vyas, P., Fuchs, P. A. and Glowatzki, E.** (2016). GluA2-
899 Containing AMPA Receptors Distinguish Ribbon-Associated from Ribbonless Afferent Contacts
900 on Rat Cochlear Hair Cells. *eNeuro* **3**.
901 **Meers, M. P., Bryson, T. D., Henikoff, J. G. and Henikoff, S.** (2019a). Improved CUT&RUN chromatin
902 profiling tools. *Elife* **8**.
903 **Meers, M. P., Tenenbaum, D. and Henikoff, S.** (2019b). Peak calling by Sparse Enrichment Analysis for
904 CUT&RUN chromatin profiling. *Epigenetics Chromatin* **12**, 42.
905 **Micucci, J. A., Sperry, E. D. and Martin, D. M.** (2015). Chromodomain helicase DNA-binding proteins in
906 stem cells and human developmental diseases. *Stem Cells Dev* **24**, 917-926.
907 **Millard, C. J., Varma, N., Saleh, A., Morris, K., Watson, P. J., Bottrill, A. R., Fairall, L., Smith, C. J. and**
908 **Schwabe, J. W.** (2016). The structure of the core NuRD repression complex provides insights
909 into its interaction with chromatin. *Elife* **5**, e13941.
910 **Morra, R., Lee, B. M., Shaw, H., Tuma, R. and Mancini, E. J.** (2012). Concerted action of the PHD,
911 chromo and motor domains regulates the human chromatin remodelling ATPase CHD4. *FEBS*
912 *Lett* **586**, 2513-2521.
913 **Nitarska, J., Smith, J. G., Sherlock, W. T., Hillege, M. M., Nott, A., Barshop, W. D., Vashisht, A. A.,**
914 **Wohlschlegel, J. A., Mitter, R. and Riccio, A.** (2016). A Functional Switch of NuRD Chromatin
915 Remodeling Complex Subunits Regulates Mouse Cortical Development. *Cell Rep* **17**, 1683-1698.
916 **Pan, M. R., Hsieh, H. J., Dai, H., Hung, W. C., Li, K., Peng, G. and Lin, S. Y.** (2012). Chromodomain
917 helicase DNA-binding protein 4 (CHD4) regulates homologous recombination DNA repair, and
918 its deficiency sensitizes cells to poly(ADP-ribose) polymerase (PARP) inhibitor treatment. *J Biol*
919 *Chem* **287**, 6764-6772.
920 **Petitpre, C., Wu, H., Sharma, A., Tokarska, A., Fontanet, P., Wang, Y., Helmbacher, F., Yackle, K.,**
921 **Silberberg, G., Hadjab, S., et al.** (2018). Neuronal heterogeneity and stereotyped connectivity in
922 the auditory afferent system. *Nat Commun* **9**, 3691.
923 **Polo, S. E., Kaidi, A., Baskcomb, L., Galanty, Y. and Jackson, S. P.** (2010). Regulation of DNA-damage
924 responses and cell-cycle progression by the chromatin remodelling factor CHD4. *EMBO J* **29**,
925 3130-3139.
926 **Quinlan, A. R. and Hall, I. M.** (2010). BEDTools: a flexible suite of utilities for comparing genomic
927 features. *Bioinformatics* **26**, 841-842.
928 **Raft, S., Koundakjian, E. J., Quinones, H., Jayasena, C. S., Goodrich, L. V., Johnson, J. E., Segil, N. and**
929 **Groves, A. K.** (2007). Cross-regulation of Ngn1 and Math1 coordinates the production of
930 neurons and sensory hair cells during inner ear development. *Development* **134**, 4405-4415.
931 **Raj, A. and van Oudenaarden, A.** (2008). Nature, nurture, or chance: stochastic gene expression and its
932 consequences. *Cell* **135**, 216-226.
933 **Ramirez, F., Dundar, F., Diehl, S., Gruning, B. A. and Manke, T.** (2014). deepTools: a flexible platform
934 for exploring deep-sequencing data. *Nucleic Acids Res* **42**, W187-191.
935 **Robinson, J. T., Thorvaldsdottir, H., Winckler, W., Guttman, M., Lander, E. S., Getz, G. and Mesirov, J.**
936 **P.** (2011). Integrative genomics viewer. *Nat Biotechnol* **29**, 24-26.
937 **Ruggero, M. A., Santi, P. A. and Rich, N. C.** (1982). Type II cochlear ganglion cells in the chinchilla. *Hear*
938 *Res* **8**, 339-356.

939 **Sanders, T. R. and Kelley, M. W.** (2022). Specification of neuronal subtypes in the spiral ganglion
940 begins prior to birth in the mouse. *Proc Natl Acad Sci U S A* **119**, e2203935119.
941 **Schmiedt, R. A.** (1989). Spontaneous rates, thresholds and tuning of auditory-nerve fibers in the gerbil:
942 comparisons to cat data. *Hear Res* **42**, 23-35.
943 **Shrestha, B. R., Chia, C., Wu, L., Kujawa, S. G., Liberman, M. C. and Goodrich, L. V.** (2018). Sensory
944 Neuron Diversity in the Inner Ear Is Shaped by Activity. *Cell* **174**, 1229-1246 e1217.
945 **Sifrim, A., Hitz, M. P., Wilsdon, A., Breckpot, J., Turki, S. H., Thienpont, B., McRae, J., Fitzgerald, T. W.,**
946 **Singh, T., Swaminathan, G. J., et al.** (2016a). Distinct genetic architectures for syndromic and
947 nonsyndromic congenital heart defects identified by exome sequencing. *Nat Genet* **48**, 1060-
948 1065.
949 **Sifrim, A., Hitz, M. P., Wilsdon, A., Breckpot, J., Turki, S. H., Thienpont, B., McRae, J., Fitzgerald, T. W.,**
950 **Singh, T., Swaminathan, G. J., et al.** (2016b). Distinct genetic architectures for syndromic and
951 nonsyndromic congenital heart defects identified by exome sequencing. *Nat Genet* **48**, 1060-
952 1065.
953 **Spoendlin, H.** (1972). Innervation densities of the cochlea. *Acta Otolaryngol* **73**, 235-248.
954 **Sun, Y., Wang, L., Zhu, T., Wu, B., Wang, G., Luo, Z., Li, C., Wei, W. and Liu, Z.** (2022). Single-cell
955 transcriptomic landscapes of the otic neuronal lineage at multiple early embryonic ages. *Cell*
956 *Rep* **38**, 110542.
957 **Taberner, A. M. and Liberman, M. C.** (2005). Response properties of single auditory nerve fibers in the
958 mouse. *J Neurophysiol* **93**, 557-569.
959 **Tong, J. K., Hassig, C. A., Schnitzler, G. R., Kingston, R. E. and Schreiber, S. L.** (1998). Chromatin
960 deacetylation by an ATP-dependent nucleosome remodelling complex. *Nature* **395**, 917-921.
961 **Torchy, M. P., Hamiche, A. and Klaholz, B. P.** (2015). Structure and function insights into the NuRD
962 chromatin remodeling complex. *Cell Mol Life Sci* **72**, 2491-2507.
963 **Toriello, H. V., Reardon, W., Gorlin, R. J. and Gorlin, R. J.** (2004). *Hereditary hearing loss and its*
964 *syndromes* (2nd edn). Oxford ; New York: Oxford University Press.
965 **Torrado, M., Low, J. K. K., Silva, A. P. G., Schmidberger, J. W., Sana, M., Sharifi Tabar, M., Isilak, M. E.,**
966 **Winning, C. S., Kwong, C., Bedward, M. J., et al.** (2017). Refinement of the subunit interaction
967 network within the nucleosome remodelling and deacetylase (NuRD) complex. *FEBS J* **284**,
968 4216-4232.
969 **Watson, A. A., Mahajan, P., Mertens, H. D., Deery, M. J., Zhang, W., Pham, P., Du, X., Bartke, T.,**
970 **Zhang, W., Edlich, C., et al.** (2012). The PHD and chromo domains regulate the ATPase activity
971 of the human chromatin remodeler CHD4. *J Mol Biol* **422**, 3-17.
972 **Weiss, K., Lazar, H. P., Kurolap, A., Martinez, A. F., Paperna, T., Cohen, L., Smeland, M. F., Whalen, S.,**
973 **Heide, S., Keren, B., et al.** (2020). The CHD4-related syndrome: a comprehensive investigation
974 of the clinical spectrum, genotype-phenotype correlations, and molecular basis. *Genet Med* **22**,
975 389-397.
976 **Weiss, K., Terhal, P. A., Cohen, L., Bruccoleri, M., Irving, M., Martinez, A. F., Rosenfeld, J. A., Machol,**
977 **K., Yang, Y., Liu, P., et al.** (2016). De Novo Mutations in CHD4, an ATP-Dependent Chromatin
978 Remodeler Gene, Cause an Intellectual Disability Syndrome with Distinctive Dysmorphisms. *Am*
979 *J Hum Genet* **99**, 934-941.
980 **Williams, C. J., Naito, T., Arco, P. G., Seavitt, J. R., Cashman, S. M., De Souza, B., Qi, X., Keables, P.,**
981 **Von Andrian, U. H. and Georgopoulos, K.** (2004). The chromatin remodeler Mi-2beta is
982 required for CD4 expression and T cell development. *Immunity* **20**, 719-733.

983 **Winter, I. M., Robertson, D. and Yates, G. K.** (1990). Diversity of characteristic frequency rate-intensity
984 functions in guinea pig auditory nerve fibres. *Hear Res* **45**, 191-202.
985 **Xia, L., Huang, W., Bellani, M., Seidman, M. M., Wu, K., Fan, D., Nie, Y., Cai, Y., Zhang, Y. W., Yu, L. R.,**
986 **et al.** (2017). CHD4 Has Oncogenic Functions in Initiating and Maintaining Epigenetic
987 Suppression of Multiple Tumor Suppressor Genes. *Cancer Cell* **31**, 653-668 e657.
988 **Xue, Y., Wong, J., Moreno, G. T., Young, M. K., Cote, J. and Wang, W.** (1998). NURD, a novel complex
989 with both ATP-dependent chromatin-remodeling and histone deacetylase activities. *Mol Cell* **2**,
990 851-861.
991 **Yang, Y., Yamada, T., Hill, K. K., Hemberg, M., Reddy, N. C., Cho, H. Y., Guthrie, A. N., Oldenborg, A.,**
992 **Heiney, S. A., Ohmae, S., et al.** (2016). Chromatin remodeling inactivates activity genes and
993 regulates neural coding. *Science* **353**, 300-305.
994 **Yoshida, T., Hu, Y., Zhang, Z., Emmanuel, A. O., Galani, K., Muhire, B., Snippert, H. J., Williams, C. J.,**
995 **Tolstorukov, M. Y., Gounari, F., et al.** (2019). Chromatin restriction by the nucleosome
996 remodeler Mi-2beta and functional interplay with lineage-specific transcription regulators
997 control B-cell differentiation. *Genes Dev* **33**, 763-781.
998 **Zhang, K. D. and Coate, T. M.** (2017). Recent advances in the development and function of type II spiral
999 ganglion neurons in the mammalian inner ear. *Semin Cell Dev Biol* **65**, 80-87.
1000 **Zhang, Y., LeRoy, G., Seelig, H. P., Lane, W. S. and Reinberg, D.** (1998). The dermatomyositis-specific
1001 autoantigen Mi2 is a component of a complex containing histone deacetylase and nucleosome
1002 remodeling activities. *Cell* **95**, 279-289.
1003 **Zhu, L. J., Gazin, C., Lawson, N. D., Pages, H., Lin, S. M., Lapointe, D. S. and Green, M. R.** (2010).
1004 ChIPpeakAnno: a Bioconductor package to annotate ChIP-seq and ChIP-chip data. *BMC*
1005 *Bioinformatics* **11**, 237.
1006